processes

MDPI

Article

Narrowband Internet of Things over Non-Terrestrial Networks for Remote Renewable-Energy Management: Architecture and Performance Evaluation

Kahraman Zaim [1,2,*], Seyit Karatepe [2] and Murat Yücel [3,4]

[1] Department of Electrical and Electronics Engineering, Institute of Science, Gazi University, 06560 Ankara, Türkiye
[2] Türk Telekomünikasyon AŞ, 06103 Ankara, Türkiye; seyit.karatepe@turktelekom.com.tr
[3] Department of Electrical and Electronics Engineering, Faculty of Technology, Gazi University, 06560 Ankara, Türkiye
[4] YIMI Electronics & Communication Co., Gazi Teknopark, 06830 Ankara, Türkiye
* Correspondence: kahraman.zaim@turktelekom.com.tr or 24833004007@gazi.edu.tr

Abstract

Reliable communication is essential for monitoring and supervisory operation of renewable-energy facilities beyond terrestrial-network coverage. This study proposes a four-layer Internet of Things (IoT) architecture aligned with 3GPP Release 17, integrating sensors, an edge gateway, Narrowband IoT (NB-IoT) access through a transparent satellite payload, terrestrial core-network functions, and centralized IoT, Energy Management System (EMS), and Supervisory Control and Data Acquisition (SCADA) applications. A 3GPP-aligned analytical framework evaluates satellite geometry, transparent-path propagation delay, deterministic uplink and downlink margins, and pass-level outage probability for Low Earth Orbit (LEO) satellites at 600 and 1200 km, medium Earth orbit (MEO) at 10,000 km, and geostationary Earth orbit (GEO) at 35,786 km, complemented by a waveform-level Narrowband Physical Downlink Shared Channel (NPDSCH) reliability experiment for a representative LEO-600 downlink. At a 50° elevation angle, the one-way satellite-induced propagation delay ranges from 5.08 ms (LEO-600) to 247.35 ms (GEO). With single transmission, the uplink is the limiting direction and does not achieve link closure in any evaluated scenario. The LEO downlinks achieve positive margins at sufficiently high elevation angles. A 1% pass-averaged outage probability requires approximately 17 dB of uplink coverage enhancement for LEO-600, whereas the MEO and GEO requirements exceed the standardized repetition range. Realized NPDSCH repetition gains (approximately 5.5 and 9 dB for 8 and 32 repetitions) remain below the ideal values. The findings identify the link-budget and delay conditions under which NTN-assisted IoT may support periodic monitoring, alarm and maintenance traffic, and non-time-critical supervisory communication, while protection functions remain local.

Keywords: non-terrestrial networks (NTNs); narrowband Internet of Things (NB-IoT); renewable energy management; satellite IoT; remote monitoring and supervisory control

Check for updates

Academic Editor: Yo-Ping Huang

Received: 29 August 2026
Revised: 24 September 2026
Accepted: 1 October 2026
Published: 10 October 2026

Copyright: © 2026 by the authors. Licensee MDPI, Basel, Switzerland. This article is an open access article distributed under the terms and conditions of the Creative Commons Attribution (CC BY) license.

1. Introduction

The development of green energy is undergoing a major transformation. There is a strong global push to reduce carbon emissions, mitigate global warming, and achieve

net-zero targets. Major forms of sustainable green energy include desert-based solar arrays, offshore wind farms, and remote hydroelectric systems [1]. Renewable-energy generation typically requires reliable communication systems at the project site. However, many locations with high renewable-energy potential are situated in remote and isolated areas, such as offshore regions [2] and sparsely populated communities [3], where conventional telecommunication infrastructure is technically difficult or economically prohibitive to deploy.

Efficient management of distributed green-energy systems [4] requires communication infrastructure capable of supporting remote data acquisition and monitoring, supervisory control, and predictive maintenance [5]. Traditional terrestrial communication networks, including fiber-optic backhaul, microwave relay links, and cellular networks, may provide insufficient coverage for distributed energy systems located in remote or geographically constrained areas [6]. Many renewable-energy facilities are situated in challenging environments, including offshore waters and mountainous regions. Deploying terrestrial infrastructure, such as subsea fiber or line-of-sight microwave links, in these environments may involve substantial technical difficulty and cost [7]. Economic constraints further motivate the need for alternative connectivity solutions in remote or uninhabited regions. The high capital expenditure (CAPEX) of deploying base stations and the operational expenditure (OPEX) associated with maintaining infrastructure in inaccessible areas create significant coverage gaps and make terrestrial networks impractical for supporting remote IoT sensors and distributed energy systems reliably [8]. Furthermore, terrestrial systems are susceptible to damage during natural disasters, including hurricanes, floods, and earthquakes [9]. Physical damage to communication links may leave green-energy facilities without remote monitoring or supervisory-control capability [10]. This loss of visibility is particularly critical for distributed generation units and microgrids that depend on coordinated power-management strategies [11], and it can create systemic risks for the wider energy infrastructure, including cascading failures [12].

Non-terrestrial network (NTN) technologies, including Low Earth Orbit (LEO), Medium Earth Orbit (MEO), and Geostationary Earth Orbit (GEO) satellite systems aligned with 3GPP standards, can address these physical and economic limitations [13] by providing wide-area and ubiquitous connectivity [14]. In particular, 3GPP Release 17 introduced standardized support for Narrowband Internet of Things (NB-IoT) and enhanced Machine-Type Communication (eMTC/LTE-M) over NTNs, enabling low-power IoT connectivity through satellite-based communication systems [15].

The NTN architecture can employ a transparent, or bent-pipe, payload in which the satellite primarily relays signals between the user equipment and the terrestrial network without extensive onboard processing. This approach is suitable for extending IoT connectivity to remote and geographically constrained green-energy facilities where terrestrial infrastructure is unavailable or unreliable. In the proposed architecture, individual sensors are not modeled as direct satellite terminals. Instead, an edge gateway aggregates data from multiple sensors and operates as the NB-IoT NTN terminal for satellite communication. Although the standardized IoT-NTN framework supports both NB-IoT and LTE-M/eMTC, the proposed architecture and numerical evaluation in this study focus on NB-IoT connectivity over the NTN link.

The first group of relevant studies addresses satellite configurations, transmission paths, and latency-related metrics in 3GPP-oriented NTN scenarios. 3GPP TR 38.811 defines fundamental NTN reference scenarios and examines satellite-related parameters such as propagation distance, elevation angle, differential delay, Doppler shift, propagation delay, and NTN-specific channel characteristics [16]. Subsequently, 3GPP TR 38.821 evaluates additional NTN reference scenarios and the effects of long propagation delays on radio-

interface timing and protocol procedures. In particular, the report investigates GEO and LEO configurations with different satellite altitudes, beam footprints, propagation delays, and delay variations, and describes enhanced timing-advance mechanisms for NTN systems [17]. For IoT-oriented NTN deployments, 3GPP TR 36.763 applies these considerations to NB-IoT and eMTC and provides reference parameters for propagation delay, differential delay, Doppler shift, Doppler variation, and other timing aspects in GEO and LEO scenarios [15]. Together, these reports provide the fundamental system-level parameters required to assess the feasibility and performance of NB-IoT-based NTN connectivity.

Conti et al. evaluated the link budget and coverage feasibility of NB-IoT over NTNs by assessing how multibeam downlink and multiuser uplink interference affect the carrier-to-interference-plus-noise ratio (CINR) in single- and multisatellite constellations [18]. Kodheli et al. investigated the performance degradation caused by differential Doppler shifts among ground users, which can impair uplink synchronization and subcarrier orthogonality in NB-IoT over LEO satellite systems, and proposed resource-allocation approaches to mitigate this effect [19].

Although NTN geometry, propagation, delay, and physical-link performance have been extensively characterized in the 3GPP study items (TR 36.763 [15], TR 38.811 [16], and TR 38.821 [17]), and link-budget [18] and Doppler-related synchronization [19] analyses have been reported, existing research has primarily focused on general NTN scenarios and communication-performance metrics. Comparatively limited attention has been given to connecting these communication characteristics with practical remote green-energy scenarios and end-to-end architectures based on 3GPP solutions. Application-oriented studies are, therefore, required in which sensing, edge processing, NTN-IoT connectivity, and link feasibility are considered together under representative conditions for geographically distributed green-energy installations.

Accordingly, the research question driving this study is as follows: under standardized 3GPP Release 17 IoT-NTN reference parameters, which orbital configurations, elevation angles, and coverage-enhancement settings allow a single edge gateway at a remote renewable-energy site to support periodic monitoring, alarm and maintenance traffic, and supervisory control, and which functions must remain local to the site?

This question is decomposed into three sub-questions: (RQ1) how large are the satellite-induced propagation delays across LEO, MEO, and GEO reference scenarios, and how do NB-IoT repetitions and access procedures add to them; (RQ2) which link direction limits bidirectional connectivity under the 3GPP reference link budgets, and by how much; and (RQ3) how much of the resulting deficit can be recovered by NB-IoT repetitions when fading, Doppler, and practical channel estimation are included. The novelty of this work does not lie in a new link-budget formula or a new physical-layer algorithm. Instead, it lies in (a) mapping standardized IoT-NTN performance metrics onto the traffic and delivery-time classes of renewable-energy monitoring and supervisory systems; (b) combining an analytical multi-orbit link budget with a waveform-level reliability experiment and an explicit parameter mapping between the two; and (c) deriving application-level guidance on which energy-management functions can be assigned to the NTN link, together with the associated latency, integration, and cost–benefit considerations.

The objective of this study is to assess a four-layer NTN-IoT framework for remote renewable-energy facilities using 3GPP-aligned models and reference parameters. The proposed framework connects distributed monitoring and control systems through an edge-assisted NTN-IoT communication platform, as illustrated in Figure 1. The main contributions of this study are as follows: (i) a four-layer architecture aligned with 3GPP IoT-NTN principles is defined, integrating remote sensors, an edge gateway, transparent satellite access, terrestrial E-UTRAN/EPC functions, and Energy Management System

(EMS)/Supervisory Control and Data Acquisition (SCADA) components; (ii) a unified analytical evaluation framework is formulated to compare Earth-curvature-aware slant range, one-way transparent-path propagation delay, propagation RTT, and deterministic uplink and downlink NB-IoT margins across LEO-600, LEO-1200, MEO-10,000, and GEO-35,786 reference scenarios over a range of elevation angles, from which the pass-level outage probability and the required coverage-enhancement gain are derived under the elevation-dependent shadowing model of 3GPP TR 38.811; (iii) a waveform-level NPDSCH experiment is conducted for a representative LEO-600 downlink to evaluate transport-block reliability under Rician fading, Doppler effects, and selected repetition counts, and its configured transmit power is explicitly mapped to the 3GPP satellite EIRP density used in the analytical link budget; and (iv) the results are translated into an air-interface latency budget that includes repetitions, random access, and timing advance, an integration approach for existing renewable-energy SCADA/EMS systems, and a cost–benefit discussion of NTN connectivity. The combined analytical and waveform-level results are interpreted in terms of periodic monitoring, alarm and maintenance traffic, and non-time-critical supervisory communication, while time-critical protection functions are retained locally. The numerical assessment considers a representative fixed edge gateway, NB-IoT connectivity, transparent NTN operation, and 3GPP-based reference parameters.

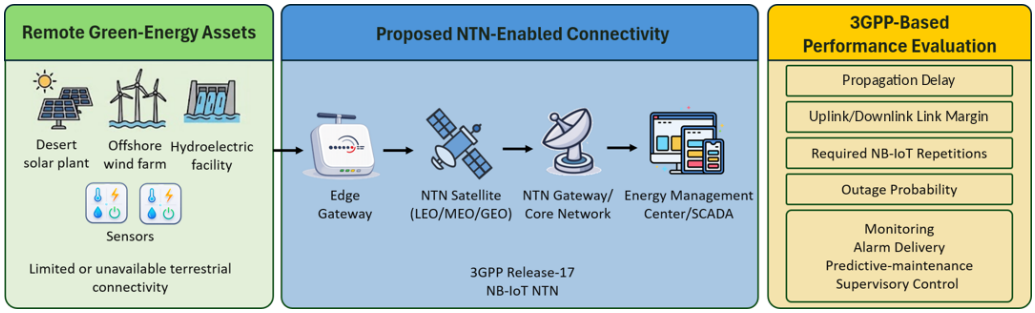


Figure 1. Scope and evaluation framework for NTN-enabled remote green-energy systems.

The remainder of this paper is organized as follows. Section 2 provides the technical background and reviews related work. Section 3 presents the proposed NTN-enabled IoT architecture. Section 4 describes the analytical system model and simulation methodology. Section 5 presents and discusses the numerical results, while Section 6 summarizes the main findings and outlines directions for future research.

2. Background and Related Work

2.1. Communication Requirements of Remote Green-Energy Systems

Green energy refers to energy harvested from environmentally friendly and renewable natural resources [20], including wind, waves, geothermal heat, sunlight, and hydrological resources [21]. Its primary objective is to reduce environmental impact while supporting sustainable electricity and heat generation. Solar, wind, and hydroelectricity are among the most widely deployed renewable-energy technologies, while bioenergy and geothermal energy also contribute to the energy mix in many countries. As environmental challenges and climate change intensify, the transition to clean energy is increasingly important for ecosystem protection and energy independence [22].

Green-energy facilities are deployed across geographically diverse and often remote environments, including desert-based and large-scale solar farms, offshore [23] and mountainous wind farms [24], remote dams and hydroelectric plants, geothermal facilities in volcanic regions [25], and rural biomass-production sites. Despite their differences, these environments share characteristics such as wide geographical distribution, difficult physical

access, harsh operating conditions, and limited terrestrial communication infrastructure. Continuous visibility of these distributed assets, therefore, depends increasingly on sensing and remote data-acquisition capabilities [26], which are essential for collecting operational measurements and maintaining reliable monitoring and control beyond the practical reach of conventional terrestrial networks [6].

Remote solar photovoltaic, wind, hydroelectric, geothermal, and biomass facilities generate heterogeneous data through environmental sensors, electrical measurement units, equipment condition-monitoring devices, and supervisory-control systems. These data include environmental and resource variables, such as solar irradiance, wind speed, water level, temperature, pressure, and flow; electrical variables, such as voltage, current, energy consumption, and power output; equipment-health indicators, such as component temperature and vibration; and operational information, including equipment status and fault indicators. The relevance and characteristics of the collected data vary according to the energy-generation technology. Photovoltaic monitoring systems primarily acquire irradiance, module temperature, and DC/AC electrical quantities through data loggers and inverter interfaces [26]. Wind-turbine SCADA systems typically report 10-min averaged operational and condition-monitoring records, which are widely used for fault detection [27]. Hydropower condition-monitoring systems focus on vibration, temperature, and hydraulic quantities of turbines and generators [28], whereas geothermal installations require temperature, pressure, and flow sensing under harsh chemical and thermal conditions [29]. Biomass plants likewise rely on SCADA-based production data for output estimation and operational planning [30].

The resulting communication traffic can be divided into three principal categories. Periodic monitoring supports routine observation of environmental, electrical, and operational conditions. Alarm and maintenance traffic includes event-driven transmission of faults, threshold violations, and abnormal conditions, as well as equipment-health indicators used for condition assessment and failure prediction. Finally, supervisory control supports the remote transmission of commands to equipment such as inverters, turbines, pumps, valves, and gates. These traffic classes have different requirements in terms of delay, reliability, data volume, reporting frequency, and link availability.

The representative operating environments, monitored variables, and communication priorities of remote green-energy systems are summarized in Table 1. To provide a quantitative basis for comparison, Table 2 additionally lists indicative reporting intervals, payload sizes, and delivery-time targets for each traffic class. The delivery-time targets are expressed using the transfer-time classes of IEC 61850-5 for power-utility automation [31], ranging from TT0 (>1000 ms) for files and logs to TT6 (3 ms) for trips and blockings. These values are used in Section 5 as reference points for the evaluated propagation and air-interface delays.

Selecting an appropriate satellite system for renewable-energy monitoring requires consideration of both the operating environment and the communication requirements of the facility. Satellite altitude, propagation delay, mobility, coverage, and link-budget characteristics affect the suitability of LEO, MEO, and GEO systems for remote IoT applications. A well-matched satellite architecture can support IoT integration, remote monitoring and control, and the operational resilience of distributed energy systems. NB-IoT is a suitable candidate for low-data-rate periodic monitoring and alarm telemetry, particularly for remote energy assets requiring low-power, wide-area connectivity. Nevertheless, NTNs should not be considered a universal replacement for terrestrial networks [32]. Instead, it provides complementary connectivity in remote, underserved, or geographically uncovered areas where terrestrial infrastructure is unavailable or limited, a role also envisaged for other non-terrestrial platforms such as high-altitude platform systems [33]. Accordingly,

this study does not assume the universal superiority of a specific satellite orbit; it evaluates NTN-based IoT connectivity according to the communication requirements of diverse remote energy assets. These requirements motivate the use of standardized IoT-NTN connectivity, whose technical evolution and related performance studies are reviewed in Section 2.2.

Table 1. Communication requirements of remote green-energy systems.

Energy Asset	Representative Remote Environment	Monitored Variables	NTN-Supported Function	Dominant Requirement
Solar PV	Deserts and vast open terrain	Irradiance, panel temperature, voltage, current, and inverter status	Periodic monitoring, fault alarms, and maintenance data	Scalability, low-power operation, and reliable alarm delivery
Wind energy	Mountainous and offshore regions	Vibration, temperature, power output, gearbox condition, and turbine status	Predictive-maintenance telemetry, alarm reporting, and supervisory control	Wide-area coverage, link availability, and bidirectional communication
Hydroelectric energy	Remote dams, rivers, and valleys	Water level, pressure, flow, turbine temperature, and equipment status	Monitoring, alarm reporting, and supervisory intervention	Reliability, coverage, and bounded communication delay
Geothermal energy	Volcanic regions and fault-line areas	Temperature, pressure, flow rate, and equipment condition	Continuous condition monitoring and alarm delivery	Reliable telemetry and infrastructure resilience
Biomass energy	Rural, agricultural, and forestry areas	Feedstock level, digester condition, gas level, and production data	Periodic telemetry, logistics coordination, and maintenance reporting	Wide-area coverage and delay-tolerant, low-rate connectivity

Table 2. Indicative quantitative traffic parameters per traffic class for remote green-energy systems.

Traffic Class	Typical Reporting Interval	Indicative Payload per Report	Indicative Delivery-Time Target	Communication Path
Periodic monitoring	1–15 min (e.g., 10-min averaged wind SCADA records)	50–500 bytes (aggregated measurements)	>1 s; TT0 class	NTNs; delay tolerant; all orbits
Alarm and maintenance	Event driven	20–200 bytes (event code, time stamp, value)	≤1 s desirable (TT1); a few seconds acceptable	NTNs; low-delay orbit preferred
Supervisory control	On demand	10–100 bytes command plus status response	0.5 s (TT2) for operator commands; a few seconds for remote supervision	NTNs; bidirectional (DL command, UL response)
Protection and emergency shutdown	Event driven	Not applicable	3–10 ms (TT5–TT6)	Local only; not assigned to NTN

Note: Time-critical protection and emergency-shutdown functions are assumed to be executed locally. NTN connectivity supports remote monitoring, alarm delivery, maintenance, and supervisory operation. Reporting intervals and payload sizes are indicative engineering assumptions used for dimensioning; delivery-time targets refer to the IEC 61850-5 transfer-time classes (TT0: >1000 ms; TT1: 1000 ms; TT2: 500 ms; TT5: 10 ms; TT6: 3 ms) [31], which were defined for power-utility automation networks and are used here only as reference points.

2.2. 3GPP IoT-NTN Standardization and Related Studies

Although terrestrial networks have evolved substantially, they retain inherent limitations in deployment feasibility [32] and cost-effectiveness [33] when serving uncovered or underserved geographical areas. Ground-based infrastructure may be impractical, expensive, or physically impossible to deploy across remote regions, oceans, and difficult terrain. As the demand for reliable and ubiquitous connectivity grows, driven partly by the increasing number of connected devices [34], NTNs have emerged as a critical means of complementing terrestrial coverage and of extending it to energy-constrained remote IoT devices [35].

NTNs are wireless communication systems in which network components are deployed on airborne or spaceborne platforms rather than exclusively on the Earth's surface [36]. Architecturally, NTN platforms can be classified into airborne and spaceborne categories according to their operating altitude [37]. This study focuses on spaceborne networks comprising satellites in different orbital regimes. GEO satellites operate at an altitude of approximately 35,786 km above the equator and rotate synchronously with the Earth, appearing stationary relative to a ground observer and providing very large coverage footprints. MEO systems operate at intermediate altitudes, typically between 8000 and 20,000 km in the scenarios considered here, while LEO satellites generally operate between approximately 500 and 2000 km. The lower altitudes of LEO and MEO systems reduce propagation distance but require moving satellite constellations. Orbital motion, therefore, introduces time-varying visibility, Doppler shift, and handover requirements, with Doppler effects being particularly significant for rapidly moving LEO satellites. A representative comparison of the orbital technologies considered in this study, compiled from the survey in [38] and the orbit characteristics summarized in [36], is provided in Table 3.

Table 3. Representative comparison of LEO, MEO, and GEO orbital technologies.

Parameter	LEO	MEO	GEO
Altitude	500–2000 km	8000–20,000 km	35,786 km
Representative end-to-end latency	Medium (20–50 ms)	High (50–150 ms)	Very high (400–700 ms)
Earth coverage	Large	Very large	Continental
Beam-footprint size	100–1000 km	100–1000 km	200–3500 km
Apparent orbital behavior	Moving, circular orbit	Moving, circular orbit	Fixed relative to the ground
Representative coverage area	Regional	Wide regional or multicountry	Country or continent scale

A NTN provides connectivity for IoT and machine-to-machine applications in remote locations beyond terrestrial cellular coverage. In 3GPP Release 17, NTN support was developed through two principal technology tracks: NR-NTN, which extends 5G NR to non-terrestrial networks, and IoT-NTN, which supports NB-IoT and eMTC using the LTE/E-UTRAN framework. This study uses 3GPP TR 36.763 as the principal standardization reference for NB-IoT over NTNs because it addresses the adaptation of LTE-based IoT technologies to satellite operation [15]. 3GPP TR 38.811 is used as a supplementary reference for satellite geometry, propagation, and NTN channel characteristics [16], whereas 3GPP TR 38.821 primarily addresses NR-NTN solutions and associated radio-interface procedures [17]. Release 18 and Release 19 subsequently introduced additional NTN and IoT-NTN enhancements; however, Release 17 is adopted as the baseline in this study because it provides mature reference parameters and reproducible NB-IoT link-budget scenarios.

Kodheli et al. investigated the link budget of satellite-based NB-IoT systems through analytical evaluation and numerical simulation, considering parameters such as satellite altitude, effective isotropic radiated power (EIRP), gain-to-noise-temperature ratio (G/T), free-space path loss, and carrier-to-noise ratio (C/N). Their study compared LEO and GEO configurations and demonstrated the influence of orbit selection on spectral efficiency, delay, capacity, and energy consumption [39]. Conti et al. conducted an NB-IoT NTN link-budget analysis for LEO satellites at 600 km and 1200 km and for GEO satellite architectures operating in the S-band. Their results showed that full-frequency-reuse scenarios can suffer from low CINR owing to interbeam interference, whereas a three-frequency reuse scheme can provide acceptable uplink and downlink performance [18]. Guidotti et al. analyzed

link-budget and CINR performance for LEO and GEO satellite systems operating with transparent payloads in the Ka-band within a 3GPP NR-NTN context. Using multibeam coverage geometry and Monte Carlo simulations, they showed that reuse factors of three and four can substantially improve CINR relative to full frequency reuse [40].

Analytical and numerical link-budget studies assess the feasibility and reliability of satellite connectivity by accounting for parameters such as satellite altitude, elevation angle, EIRP, antenna characteristics, free-space path loss, C/N, link margin, and uplink/downlink asymmetry. Comparing LEO, MEO, and GEO configurations provides a direct means of assessing how satellite altitude and propagation conditions affect link feasibility. The present study adopts the established link-budget methodology and commonly used 3GPP reference parameters, while shifting the application focus toward reliable communication for remote green-energy facilities.

Adapting these IoT-NTN protocols to renewable-energy applications raises additional challenges that generic NTN link-budget studies do not address. First, utility communication protocols such as IEC 60870-5-104 were designed for terrestrial wide-area networks and rely on TCP sessions, acknowledgement windows, and application-layer timers [41]; these timers can expire when satellite RTT and repetition-induced delays consume part of the protocol/application timing budget and may require adjustment of polling intervals or implementation-specific timers in deployments configured for tighter response times. Second, the overhead of TCP/IP, transport-layer security, and SCADA framing is large relative to the few tens to hundreds of bytes carried by an NB-IoT transport block; lightweight publish/subscribe or request/response protocols such as MQTT [42] and CoAP [43], together with header compression or non-IP data delivery, are, therefore, preferable on the satellite segment. Third, supervisory commands are downlink-initiated, whereas NB-IoT terminals conserve energy through power-saving mode and extended discontinuous reception, which delay the reachability of the terminal [34]. Fourth, the security requirements of energy cyber-physical systems, including authentication, integrity protection, and segregation of control traffic, must be satisfied without saturating the narrowband link [44]. Finally, the delivery-time classes defined for power-utility automation [31] show that protection functions requiring 3–10 ms cannot be carried over any satellite orbit, whereas monitoring, event, and operator-command classes are compatible with NTNs only if propagation, repetition, and access delays are jointly bounded. These challenges motivate the edge-gateway-centric integration approach described in Section 3.2 and the latency analysis in Section 5.5.

A comprehensive NTN-IoT analysis may additionally include timing advance, synchronization, satellite visibility, handover, stochastic outage behavior, and device-energy consumption. Full handover procedures, constellation-level availability, random-access performance, and device-level energy analysis would introduce further modeling complexity and are not included in the present study; however, a single-link, pass-level outage probability is derived analytically from the margin–elevation curves (Section 5.3). Instead, the evaluation is limited to a representative static edge gateway, rural line-of-sight conditions, elevation-angle variation, analytical propagation-delay and link-budget calculations, and a waveform-level NPDSCH reliability experiment for one representative LEO downlink. Doppler effects and selected NPDSCH repetition counts are included only in this waveform-level experiment. The durations associated with repetitions, random access, and timing-advance-related scheduling offsets are, however, included analytically in the latency budget of Section 5.5. This scope provides a simplified and standards-aligned approach for assessing NTN connectivity for remote renewable-energy projects.

Research on NTN-enabled IoT has mainly addressed three areas: (i) general NTN architectures and standardization, (ii) NB-IoT link-level and link-budget feasibility,

and (iii) energy-efficiency and reliability considerations for remote IoT devices. However, limited work combines these areas within a single layered and application-oriented framework for remote green-energy management. The present study addresses this gap by combining a layered remote-energy architecture with a 3GPP-aligned evaluation of propagation delay, deterministic uplink and downlink link margins, and waveform-level NPDSCH reliability under selected repetition counts. Based on these communication requirements and standardization foundations, the proposed architecture is presented in Section 3.

3. Proposed NTN-Enabled IoT Architecture

3.1. Four-Layer Architecture and End-to-End Data Flow

The proposed architecture targets IoT connectivity between remote green-energy facilities with unavailable or insufficient terrestrial coverage and centralized energy-management systems. As shown in Figure 2, the architecture comprises four layers: the Data Acquisition and Edge Layer, Space and Access Layer, Ground Station and Core Network Layer, and Application and Control Layer. The end-to-end communication path is

Sensors → Edge Gateway → IoT-NTN Service Link → Satellite → Feeder Link → NTN Gateway/eNB → EPC → IoT Platform and EMS/SCADA.

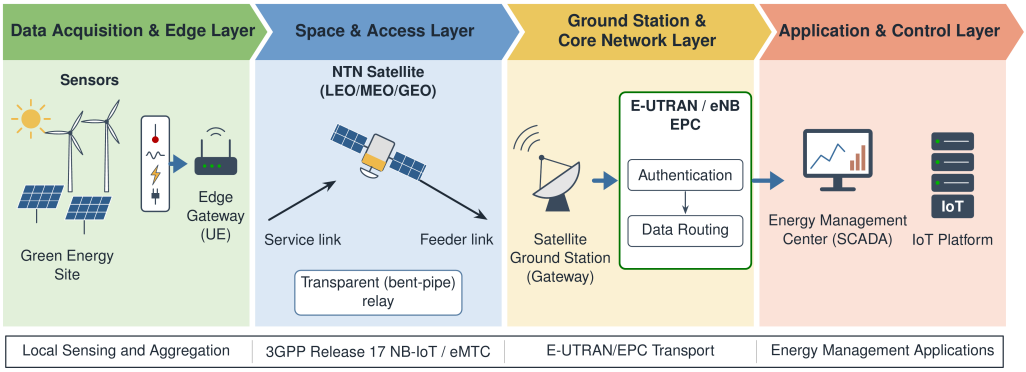


Figure 2. Proposed four-layer 3GPP-aligned NTN-IoT architecture.

The Data Acquisition and Edge Layer comprises sensors deployed at green-energy facilities to collect environmental and operational data, including electrical measurements, environmental conditions, equipment-health parameters, status information, and alarms. The sensors do not communicate directly with the satellite. Instead, an edge gateway acts as the aggregation and communication interface. The gateway performs data aggregation, basic preprocessing, timestamping, protocol adaptation, local buffering, and preparation of the collected information for transmission over the NB-IoT NTN link.

The Space and Access Layer and the Ground Station and Core Network Layer form the communication path between the remote edge gateway and the application platform. The edge gateway transmits the prepared data to the satellite through the service link. Based on 3GPP Release 17 IoT-NTN principles, the radio link supports NB-IoT connectivity over LEO, MEO, or GEO satellites, extending IoT communication beyond terrestrial-network coverage [15]. The satellite employs a transparent, or bent-pipe, payload that relays the received signals without regenerative onboard baseband processing and forwards them over the feeder link to an NTN gateway on the ground. The NTN gateway transfers the traffic to the terrestrial E-UTRAN/EPC infrastructure. The core network performs functions including authentication, mobility and session support, and packet routing toward the application platform. Consequently, the communication flow extends from

the local sensors and edge gateway through the satellite service and feeder links to the terrestrial core network and centralized applications.

The Application and Control Layer is the final stage of the architecture, where the collected data reach the IoT platform and EMS/SCADA environment at the Energy Management Center. The IoT platform provides telemetry visualization, remote monitoring, alarm processing, historical-data storage, and maintenance analytics, allowing operators to monitor the condition and performance of remote green-energy assets continuously. The processed information is used by the EMS/SCADA system for higher-level energy management and supervisory operations, including performance evaluation, anomaly detection, maintenance-decision support, and supervisory-command generation. Supervisory commands generated by the EMS/SCADA system are transmitted back to remote assets through the same communication layers. Thus, the IoT platform primarily supports data acquisition, visualization, storage, and analytics, whereas the EMS/SCADA system provides supervisory monitoring and control for distributed green-energy facilities.

3.2. Integration with Existing Renewable-Energy Monitoring and Control Systems

The proposed NTN infrastructure is not intended to replace the monitoring and control systems already installed at renewable-energy facilities. Instead, it is integrated as an additional wide-area transport path between the existing field equipment and the existing control-center applications, with the edge gateway acting as the integration point. The integration is organized at three interfaces.

3.2.1. Field-Side Interface

Inverters, turbine controllers, remote terminal units, protection relays, meters, and data loggers are connected to the edge gateway through the site's existing local interfaces, typically Modbus RTU/TCP, IEC 60870-5-101/104 [41], or IEC 61850-based substation communication [31]. The gateway acts as a protocol converter and data concentrator: it polls or subscribes to local devices at their native rates, applies deadband and report-by-exception filtering, aggregates measurements into compact messages, and time-stamps them using the global navigation satellite system (GNSS) receiver that Release 17 IoT-NTN terminals already require for timing and frequency pre-compensation [15]. Local buffering provides store-and-forward operation during link outages or satellite-visibility gaps.

3.2.2. Satellite-Segment Interface

Over the NB-IoT NTN link, the gateway uses lightweight application protocols such as MQTT [42] or CoAP [43], or non-IP data delivery through the EPC, rather than transporting the verbose native SCADA protocol end to end. Traffic is protected by end-to-end encryption and a private access-point-name or virtual-private-network configuration in the EPC, in line with the security requirements of energy cyber-physical systems [44], and alarm and command messages are assigned higher priority than periodic reports.

3.2.3. Control-Center Interface

At the Energy Management Center, the IoT platform terminates the lightweight protocol and exposes the site data to the existing SCADA/EMS through standard interfaces, for example as an IEC 60870-5-104 outstation or through an OPC UA server. Consequently, the remote site appears to the existing SCADA/EMS as a conventional remote terminal unit, and no modification of the EMS application layer is required. Because the IEC 60870-5-104 session is terminated at the IoT platform, its transport-layer timers are not exposed to the satellite path; only the SCADA polling periods and the application-level command-confirmation timeouts must accommodate the satellite round-trip, repetition, and access delays (Section 5.5), and unsolicited (spontaneous) reporting is preferred to cyclic polling.

Three deployment modes follow from this integration approach: (i) NTN as the primary link at sites without terrestrial coverage; (ii) NTN as a backup link that is activated automatically when an existing terrestrial or microwave link fails, thereby addressing the disaster-resilience requirement discussed in Section 1; and (iii) NTN as a complementary low-rate channel for alarms and supervisory messages, while high-volume data, such as raw vibration waveforms, are processed locally at the edge and only the extracted features are transmitted.

3.3. Operating Scenarios and Design Assumptions

To evaluate the proposed NTN-based IoT architecture, this study considers a representative fixed renewable-energy facility at which terrestrial communication infrastructure is unavailable or unreliable. The facility contains multiple sensors for monitoring environmental and operational parameters, and the generated data are collected by a single representative edge gateway. After aggregating the sensor data and performing basic processing, the edge gateway connects directly to the NTN infrastructure through an IoT service link. The sensor data are, therefore, transmitted to the centralized system without requiring a terrestrial base station at the remote facility.

The edge gateway is assumed to be stationary and aware of its geographical position. The communication geometry and link parameters between the gateway and satellite can, therefore, be determined using the known gateway location and satellite-orbit information. The satellite payload is modeled as transparent, meaning that it relays the received signal without regenerative onboard baseband processing. Four representative satellite scenarios are considered: LEO at 600 km, LEO at 1200 km, MEO at 10,000 km, and GEO at 35,786 km. These scenarios enable comparison of the effects of satellite altitude and elevation angle on communication distance, propagation delay, and link margin while maintaining the same fixed facility and edge-gateway assumptions. The complete numerical parameters are specified in Section 4.3.

The data exchanged between the remote renewable-energy facility and the Energy Management Center are grouped into three traffic classes: periodic monitoring traffic, alarm and maintenance traffic, and supervisory-command traffic. Periodic monitoring primarily comprises low-data-rate sensor measurements and is relatively delay tolerant because routine monitoring does not require immediate delivery of every measurement. Alarm and maintenance traffic requires greater reliability and shorter delivery time to support timely identification of abnormal conditions and maintenance events. Supervisory-command traffic requires bidirectional communication because commands generated by the EMS/SCADA system must reach the remote facility and the resulting equipment status must be reported back. Time-critical local protection and emergency-shutdown operations are excluded from these traffic classes and are assumed to be executed locally. Predictive maintenance relies on regular and reliable delivery of sensor measurements rather than continuous waveform transmission. All three traffic classes share the same physical NB-IoT connection but may be assigned different priority levels.

Satellite-orbit selection is not determined by a single characteristic such as altitude or propagation delay. The LEO-600, LEO-1200, MEO-10,000, and GEO-35,786 configurations are evaluated using multiple communication-performance metrics, including propagation distance, propagation delay, uplink margin, and downlink margin. Each orbit configuration is assessed using corresponding 3GPP-based reference parameters. The comparison, therefore, captures not only satellite altitude but also the combined effects of orbit-specific propagation and link-budget conditions on communication reliability.

The analytical model is subject to several assumptions and limitations. It evaluates a representative service link from a stationary edge gateway operating in a rural line-of-

sight environment. A minimum elevation angle is assigned to the service link, and the satellite payload is assumed to operate in transparent mode. The NTN communication scenario uses S-band IoT-NTN parameters and assumes sufficient feeder-link margin. Although feeder-link propagation distance is included in the satellite-path propagation-delay calculation, a separate feeder-link budget is not quantified because the low-power terminal service link is treated as the limiting link. Full-constellation coverage, satellite handover, network routing and queuing, detailed site-specific CAPEX/OPEX quantification, and local protection-loop simulation are outside the scope of this study; a cost–benefit discussion is provided in Section 5.6. The analytical system model and simulation methodology are presented next in Section 4.

4. System Model and Simulation Methodology

4.1. NTN Geometry and Propagation Delay Model

The service and feeder links introduced in Section 3 are mapped to the geometry shown in Figure 3. A stationary, sea-level edge gateway serves as the NB-IoT UE on a spherical Earth of radius R_E, while a transparent bent-pipe satellite is located at altitude h above the subsatellite point P_s. The UE and terrestrial NTN gateway observe elevation angles ε_u and ε_g, producing slant ranges d_{SL} and d_{FL}, respectively. The NTN gateway is co-located with the terrestrial eNB, and c denotes the speed of light.

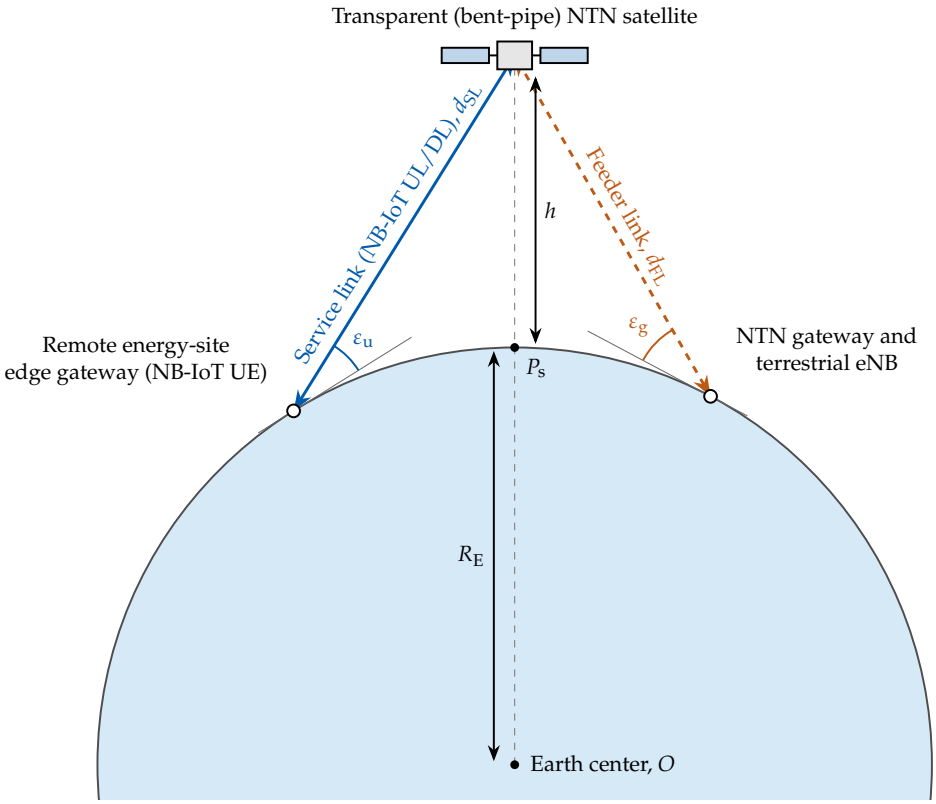


Figure 3. Geometrical and link-level system model for transparent-payload IoT NTN.

Earth curvature is retained by expressing the satellite-to-ground slant range as a function of satellite altitude and elevation angle. Following the geometry specified in 3GPP TR 38.811 [16], the slant range is

$$d(h, \varepsilon) = \sqrt{(R_E \sin \varepsilon)^2 + h^2 + 2R_E h} - R_E \sin \varepsilon, \quad (1)$$

where the square root applies to the three terms $(R_E \sin\varepsilon)^2$, h^2, and $2R_E h$ only, and $R_E \sin\varepsilon$ is subtracted outside the root. For example, $h = 600$ km and $\varepsilon = 50^\circ$ give $d = 760.82$ km, and $\varepsilon = 90^\circ$ gives $d = h$, as expected.

Accordingly, the service- and feeder-link distances are obtained as $d_{SL} = d(h, \varepsilon_u)$ and $d_{FL} = d(h, \varepsilon_g)$, respectively. Equation (1) is applied without modification to the LEO-600, LEO-1200, MEO-10,000, and GEO-35,786 scenarios. The LEO configurations follow representative NB-IoT NTN link-budget cases [18], whereas the MEO and GEO altitudes are consistent with the NTN reference cases in 3GPP TR 38.811 [16].

For the transparent-payload configuration, the one-way satellite-induced propagation delay is the sum of the service- and feeder-link propagation times, while the propagation round-trip time corresponds to twice this value [16]. Thus,

$$\begin{aligned} \tau_{prop} &= \frac{d_{SL} + d_{FL}}{c}, \\ RTT_{prop} &= 2\tau_{prop} = \frac{2(d_{SL} + d_{FL})}{c}. \end{aligned} \tag{2}$$

The quantities in Equation (2) represent only the propagation delay introduced by the satellite path. NB-IoT scheduling, transmission repetitions, satellite and gateway processing, queuing, terrestrial core-network transport, and application-layer processing are excluded. Consequently, the numerical results are reported as propagation delay rather than end-to-end latency.

4.2. 3GPP-Based Link-Budget Model

The link-budget evaluation is restricted to the NB-IoT service link because the feeder link is assumed to provide sufficient margin, as specified in Section 3.3. For each direction $\ell \in \{UL, DL\}$, the slant range d_{SL} is obtained from Equation (1), while f_ℓ and B_ℓ denote the corresponding carrier frequency and channel bandwidth. The satellite EIRP-density and receiver G/T values are selected from 3GPP TR 36.763 [15], and the large-scale propagation terms follow 3GPP TR 38.811 [16]. The free-space path loss is calculated as

$$L_{FS,\ell}(\varepsilon_u) = 20\log_{10}\left(\frac{4\pi f_\ell d_{SL}(\varepsilon_u)}{c}\right), \tag{3}$$

where d_{SL} is expressed in meters and f_ℓ in hertz. The total service-link loss is represented by

$$L_{tot,\ell} = L_{FS,\ell} + L_{atm,\ell} + L_{scin,\ell} + L_{cl,\ell} + L_{pol,\ell} + L_{add,\ell} + L_{sh,\ell}, \tag{4}$$

where the additional terms denote atmospheric absorption, scintillation, clutter, polarization, implementation or miscellaneous loss, and the fixed shadow margin, respectively. Building-entry loss is excluded for the outdoor terminal, and $L_{cl,\ell} = 0$ under the adopted rural-LOS condition.

The shadow margin $L_{sh} = 3$ dB and the scintillation loss $L_{scin} = 2.2$ dB are applied as elevation-independent constants in Equation (4). These values follow the 3GPP NTN link-budget calibration [17] and are justified as follows. For the rural and suburban LOS scenario in the S-band, 3GPP TR 38.811 models shadow fading as a zero-mean log-normal variable whose standard deviation is $\sigma_{SF}(\varepsilon) = 1.79, 1.14, 1.14, 0.92, 1.42, 1.56, 0.85, 0.72$, and 0.72 dB at $\varepsilon = 10^\circ, 20^\circ, \ldots, 90^\circ$, respectively [16]. The rural-LOS shadowing is, therefore, weak and not monotonic in elevation, and the fixed 3-dB margin exceeds the 95th-percentile shadowing loss $1.645\,\sigma_{SF}(\varepsilon)$ at every elevation angle (the largest value is 2.94 dB at 10°). The constant shadow margin is, thus, a conservative, rather than an optimistic, representation of elevation-dependent shadowing. The land-mobile-satellite statistics of ITU-R P.681 [45], which describe roadside-tree and building shadowing for moving terminals,

are not adopted because the gateway antenna is fixed and can be installed with a clear view of the sky. For the scintillation term, TR 38.811 models the ionospheric scintillation loss below 6 GHz as $6.22\, f^{-1.5}$ dB with f in GHz, independently of the elevation angle, which yields 2.2 dB at 2 GHz, whereas its elevation-dependent tropospheric-scintillation model is applied only above 6 GHz [16]. Because ionospheric scintillation is strongest in low-latitude regions, this value is conservative for mid-latitude sites. Consequently, in the rural-LOS S-band case, shadowing is the only elevation-dependent large-scale term, and its effect on the crossing angles and on the outage probability is quantified in Section 5.3 using $\sigma_{\mathrm{SF}}(\varepsilon)$.

For each link direction, the transmitter EIRP and receiver figure of merit are assigned according to whether the UE or satellite acts as the transmitter. When satellite EIRP is specified as a spectral density, it is converted to the selected channel bandwidth before the link budget is evaluated. Using the satellite-link formulation in 3GPP TR 38.821 [17], the received carrier-to-noise ratio in decibels is

$$\gamma_\ell = \left(\frac{C}{N}\right)_\ell = \mathrm{EIRP}_\ell + \left(\frac{G}{T}\right)_{\mathrm{r},\ell} - L_{\mathrm{tot},\ell} - k_{\mathrm{dB}} - 10\log_{10} B_\ell, \tag{5}$$

where $k_{\mathrm{dB}} = -228.6$ dBW/K/Hz is Boltzmann's constant in logarithmic units. The required CNR of each direction is obtained from a reference E_b/N_0 by accounting for the modulation order, effective code rate, occupied subcarriers, and cyclic-prefix overhead, following the MathWorks NB-IoT NTN link-budget reference model [46]:

$$\begin{aligned} \gamma_{\mathrm{req},\ell} &= \left(\frac{E_\mathrm{b}}{N_0}\right)_{\mathrm{ref}} + 10\log_{10}(mR_\ell) + 10\log_{10}\frac{N_{\mathrm{DSC}}}{N_{\mathrm{FFT}}} + 10\log_{10}\frac{T_\mathrm{d}}{T_\mathrm{d}+T_{\mathrm{CP}}}, \\ R_{\mathrm{UL}} &= \frac{N_{\mathrm{TBS}}+N_{\mathrm{CRC}}}{N_{\mathrm{RU}}N_{\mathrm{sym}}\, m\, N_{\mathrm{Rep}}}, \qquad R_{\mathrm{DL}} = \frac{N_{\mathrm{TBS}}+N_{\mathrm{CRC}}}{N_{\mathrm{SF}}N_{\mathrm{sym}}\, m\, N_{\mathrm{Rep}}}, \end{aligned} \tag{6}$$

where $m = 2$ for QPSK, $N_{\mathrm{TBS}} = 208$, $N_{\mathrm{CRC}} = 24$, $N_{\mathrm{sym}} = 160$, $N_{\mathrm{RU}} = 1$, $N_{\mathrm{SF}} = 8$, $N_{\mathrm{DSC}} = 72$, $N_{\mathrm{FFT}} = 128$, and T_d and T_{CP} correspond to 128 and 9 samples at 1.92 MHz, respectively. The larger number of downlink subframes yields a lower effective code rate and, therefore, a lower downlink threshold. For the adopted QPSK reference configuration with $N_{\mathrm{Rep}} = 1$ and $(E_\mathrm{b}/N_0)_{\mathrm{ref}} = 10.5$ dB, Equation (6) gives the analytical reference CNR thresholds $\gamma_{\mathrm{req,UL}} = 9.32$ dB and $\gamma_{\mathrm{req,DL}} = 0.29$ dB. Accordingly, the directional and limiting bidirectional link margins are

$$\begin{aligned} M_\ell &= \gamma_\ell - \gamma_{\mathrm{req},\ell}, \qquad \ell \in \{\mathrm{UL}, \mathrm{DL}\}, \\ M_{\mathrm{min}} &= \min\{M_{\mathrm{UL}}, M_{\mathrm{DL}}\}. \end{aligned} \tag{7}$$

A direction achieves link closure without additional repetitions when $M_\ell \geq 0$, whereas bidirectional connectivity requires $M_{\mathrm{min}} \geq 0$. NB-IoT repetitions are treated as a coverage-enhancement mechanism [39], consistent with their role in NPUSCH and NPDSCH [47]. However, because the realized repetition gain depends on fading, channel estimation, synchronization, and soft-combining performance, no ideal accumulation gain or deterministic required-repetition calculation is applied. Instead, the effect of selected NPDSCH repetition counts is evaluated directly through the waveform-level simulation described below.

The pass-level outage model is constructed as follows. To translate the margin–elevation curves into an outage probability, the fixed shadow margin is replaced by the elevation-dependent log-normal shadowing of TR 38.811, and the elevation angle is made time-varying according to the satellite pass. For a given elevation angle, the link of direction

ℓ is in outage when the shadowing loss exceeds the margin available before the shadow margin is deducted, i.e.,

$$P_{\mathrm{out},\ell}(\varepsilon; G_{\mathrm{CE}}) = Q\left(\frac{M_\ell(\varepsilon) + L_{\mathrm{sh}} + G_{\mathrm{CE}}}{\sigma_{\mathrm{SF}}(\varepsilon)}\right), \tag{8}$$

where $Q(\cdot)$ is the Gaussian tail function, $\sigma_{\mathrm{SF}}(\varepsilon)$ is linearly interpolated between the 10°-spaced values of TR 38.811, and G_{CE} (dB) is an additional coverage-enhancement gain, for example from repetitions, with $G_{\mathrm{CE}} = 0$ corresponding to $N_{\mathrm{Rep}} = 1$. For a circular orbit and a non-rotating Earth, the Earth-central angle between the gateway and the subsatellite point at elevation ε, and its evolution during a pass, are

$$\psi(\varepsilon) = \arccos\left(\frac{R_{\mathrm{E}} \cos\varepsilon}{R_{\mathrm{E}} + h}\right) - \varepsilon, \qquad \cos\psi(t) = \cos\psi_0 \cos(\omega_{\mathrm{s}} t), \qquad \omega_{\mathrm{s}} = \sqrt{\frac{\mu}{(R_{\mathrm{E}} + h)^3}}, \tag{9}$$

where ψ_0 is the central angle at the closest approach ($\psi_0 = 0$ for an overhead pass), $t = 0$ is the time of closest approach, and $\mu = 3.986 \times 10^{14}$ m^3/s^2 is the geocentric gravitational constant. The satellite is visible while $\psi(t) \le \psi_{\max} = \psi(\varepsilon_{\min})$ with $\varepsilon_{\min} = 10°$, i.e., for $T_{\mathrm{vis}}(\psi_0) = (2/\omega_{\mathrm{s}}) \arccos(\cos\psi_{\max} / \cos\psi_0)$. The outage probability is obtained by averaging Equation (8) over the visible time of a pass and, for the pass-averaged value, over ground-track offsets ψ_0 uniformly distributed in $[0, \psi_{\max})$:

$$\bar{P}_{\mathrm{out},\ell}(G_{\mathrm{CE}}) = \frac{\displaystyle\int_0^{\psi_{\max}} \int_{-T_{\mathrm{vis}}(\psi_0)/2}^{T_{\mathrm{vis}}(\psi_0)/2} P_{\mathrm{out},\ell}(\varepsilon(t;\psi_0); G_{\mathrm{CE}})\, \mathrm{d}t\, \mathrm{d}\psi_0}{\displaystyle\int_0^{\psi_{\max}} T_{\mathrm{vis}}(\psi_0)\, \mathrm{d}\psi_0}. \tag{10}$$

For GEO, the elevation angle is fixed by the site location, and Equation (8) is evaluated directly. The required coverage-enhancement gain is the smallest G_{CE} for which $\bar{P}_{\mathrm{out},\ell}$ does not exceed a target value; under ideal accumulation, it corresponds to at least $N_{\mathrm{Rep}} = 10^{G_{\mathrm{CE}}/10}$ repetitions, which is a lower bound because the realized repetition gain is below the ideal gain (Section 5.4). Fast (Rician) fading is not included in Equation (8) because it is addressed by the waveform-level experiment; hence, $\bar{P}_{\mathrm{out},\ell}$ is the probability that the shadowed large-scale link budget does not close. Equations (8)–(10) are evaluated by numerical integration of the analytical margins and do not involve additional waveform simulations.

4.3. Simulation Setup and Performance Metrics

The numerical evaluation comprises two complementary stages implemented in MATLAB R2026a using the Satellite Communications Toolbox and LTE Toolbox. First, an equation-based parameter sweep is performed for the propagation-delay and deterministic link-budget analyses. For each orbital scenario, the service-link elevation angle is varied from 10° to 90° in 1° increments. Equations (1)–(7) are evaluated sequentially to obtain the propagation geometry, one-way satellite-induced delay, propagation RTT, FSPL, CNR, and uplink and downlink margins. The fixed propagation losses and shadow margin are included deterministically in this stage. The slant range is computed with the circular-orbit geometry of Equation (1), and the CNR of Equation (5) is evaluated with the satelliteCNR function, whose FSPL output is used in Equation (3). The implementation follows the structure of the MathWorks NB-IoT NTN link-budget example [46], with the orbit-specific parameter sets, UE configuration, and loss terms listed in Table 4; all reported delays and margins were cross-checked against an independent closed-form evaluation of Equations (1)–(6).

The orbit-specific satellite parameters are taken from the S-band calibration sets in 3GPP TR 36.763: Set 2 is used for LEO-600, LEO-1200, and GEO-35,786, whereas Set 5 is used for MEO-10,000 [15]. The propagation geometry follows 3GPP TR 38.811 [16]. Because the MEO case belongs to a different calibration set, its comparison with the Set 2 cases represents a comparison of standardized reference scenarios rather than an identical-payload comparison. This mixed choice is dictated by the standard itself: in TR 36.763, the LEO-600, LEO-1200, and GEO cases are defined in Sets 1–3, whereas the MEO-10,000 case is defined only in Set 5, so no Set 2 MEO payload exists [15]. Set 2 was retained for the LEO and GEO cases because it provides a single, internally consistent payload class for all three altitudes and has lower EIRP density and G/T than Set 1, which makes it a conservative choice. Because Equations (5)–(7) are linear in decibels, changing the parameter set shifts the margins only by the differences in satellite EIRP density (downlink) and G/T (uplink), independently of the elevation angle. For example, using Set 1 instead of Set 2 would raise both the uplink and downlink margins of LEO-600 and LEO-1200 by 6.0 dB and the GEO downlink and uplink margins by 5.5 and 5.0 dB, respectively. Even under Set 1, the LEO-600 uplink margin would remain negative at zenith (-1.6 dB), so the identification of the uplink as the limiting direction does not depend on the selected parameter set.

The second stage is a waveform-level NPDSCH reliability experiment conducted for the representative LEO-600 downlink at 2 GHz and 50° elevation, based on the MathWorks NB-IoT NTN NPDSCH throughput reference model [48]. The transmitted waveform uses QPSK, MCS 0, a 208-bit transport block, eight NPDSCH subframes, and $N_{\mathrm{Rep}} \in \{1, 8, 32\}$. These repetition counts are selected as sensitivity cases rather than being derived from the deterministic link-margin deficits. The waveform is propagated through a Rician fading channel with a 10-dB K-factor, free-space path loss, and satellite Doppler. Transmitter-side Doppler pre-compensation is enabled, whereas receiver-side Doppler compensation is disabled; the rationale for this configuration and the resulting residual Doppler are stated explicitly below. The configured transmit power is swept from 22 to 46 dBm in 1-dB increments, and 1000 transport blocks are decoded at each power–repetition point. Transport-block reliability is reported as the percentage of blocks that pass the CRC after channel estimation, soft combining, and NPDSCH decoding.

The waveform-level processing chain is as follows. For each subframe, the transmitter generates the NB-IoT resource grid in standalone mode, including the narrowband primary and secondary synchronization signals (NPSS/NSSS), the narrowband reference signal (NRS), and the NPDSCH carrying the rate-matched and repeated transport block. The grid is OFDM-modulated at a sampling rate of 1.92 MHz and scaled to the configured transmit power P_{tx}. The satellite Doppler shift for the given altitude, elevation angle, and carrier frequency is pre-compensated at the transmitter, after which the waveform passes through an ETSI Rician fading channel with a K-factor of 10 dB and a maximum Doppler frequency of the diffuse component of approximately 5.6 Hz (see below), together with the satellite Doppler shift that the transmitter-side pre-compensation is designed to remove, and the free-space path loss at the 50° slant range. Complex white Gaussian noise with power spectral density kT_{eq}, where $T_{\mathrm{eq}} = T_{\mathrm{A}} + T_0(F-1)$, $T_{\mathrm{A}} = T_0 = 290$ K, and F is the linear noise figure, is added over the full sampling bandwidth. The receiver performs NPSS-based timing synchronization, OFDM demodulation, NRS-based least-squares channel estimation with time–frequency averaging and cubic interpolation, NPDSCH equalization, soft combining of the repetitions, and tail-biting convolutional decoding followed by the CRC check. The same random seed is used at all power points so that the curves differ only in P_{tx} and N_{Rep}.

Regarding the role of the fading Doppler parameter, the 3-km/h speed setting is inherited from the reference model [48] and does not represent motion of the gateway, which is stationary (Section 3.3). In the channel model, it determines only the maximum Doppler frequency of the diffuse (scattered) Rician component, $f_m = vf/c \approx 5.6$ Hz at 2 GHz, i.e., the temporal variability of the multipath caused by moving scatterers around a fixed antenna, such as vegetation, the sea surface, or rotating turbine blades, while the line-of-sight geometry remains fixed. This value is approximately four orders of magnitude smaller than the satellite-induced Doppler shift, $f_{d,sat} = (v_{sat}f/c)\,[R_E/(R_E + h)]\cos\varepsilon$ with $v_{sat} = \sqrt{\mu/(R_E + h)} \approx 7.56$ km/s [48], which for LEO-600 at 2 GHz is approximately 45.4, 29.6, and 0 kHz at 10°, 50°, and 90° (at the horizon, this expression approaches the maximum of approximately ±48 kHz, i.e., ±24 ppm, considered for LEO-600 at 2 GHz [17]). Hence, f_m plays no role in frequency synchronization. Its only effect on the waveform-level results (Section 5.4) is through the fading coherence time, $T_c \approx 0.423/f_m \approx 76$ ms: a single 8-ms NPDSCH transmission experiences quasi-static fading, whereas the 256-ms transmission with $N_{Rep} = 32$ spans approximately three coherence times and, therefore, obtains some time diversity, which is included in the realized repetition gains. A strictly static channel ($f_m = 0$) would, if anything, reduce the realized gain for large N_{Rep}, which would reinforce the conclusion that ideal accumulation gains should not be assumed. In Table 4, the parameter is, therefore, stated as the maximum Doppler frequency of the diffuse component.

With regard to Doppler compensation and residual Doppler, in the downlink experiment, the transmitter is the network side, i.e., the eNB transmitting through the transparent satellite. The transmitter-side pre-compensation removes the satellite Doppler shift computed from the satellite ephemeris and the gateway position; because the model applies the same value in the channel, the residual common Doppler at the gateway is zero, and the only remaining frequency dispersion is the 5.6-Hz diffuse Doppler spread, which is 3.7×10^{-4} of the 15-kHz subcarrier spacing. This configuration corresponds to Release 17 operation in which the gateway position is known (Section 3.3), the satellite ephemeris is broadcast [15], and the Doppler is pre-compensated for a reference point that coincides with the gateway. Receiver-side (NPSS-based) compensation was disabled because, with a zero residual offset, it could only add estimation noise, and because the NPSS-based estimate becomes unreliable at SNRs below approximately −10 dB [48], which includes the low-power part of the sweep (approximately −18.7 dB at 22 dBm; see Equation (11)). The waveform-level results in Section 5.4, therefore, represents ideal frequency synchronization. In a practical deployment, a residual offset remains, consisting of the differential Doppler between the gateway and the beam reference point, which for LEO-600 at 50° is approximately 40 Hz per kilometer of along-track distance (i.e., approximately 0.4 and 1.9 kHz at 10 and 50 km), together with ephemeris and GNSS errors. Such offsets are removed by the standard NPSS/NRS-based frequency tracking of the terminal; a remaining error of 100–200 Hz after tracking produces inter-carrier interference that is approximately 32–38 dB below the signal power, which is negligible at operating SNRs of approximately 0 dB. The most sensitive part of Figure 6 is the $N_{Rep} = 32$ curve, whose transition lies at SNRs of approximately −13 to −10 dB, where frequency estimation degrades; its realized repetition gain should, therefore, be interpreted as an upper bound obtained under ideal synchronization.

In the waveform model, no separate satellite transmit-antenna gain or UE receive-antenna gain is applied (the UE antenna gain is 0 dBi). Hence, the configured transmit power P_{tx} denotes the total power of the 180-kHz NB-IoT downlink carrier radiated toward the UE, that is, the satellite EIRP per NB-IoT carrier; it is neither a per-subcarrier power nor the total multi-carrier or multi-beam power of the satellite or base station. The equivalent operating point of the analytical Set 2 link budget on the P_{tx} axis is, therefore,

$$P_{\mathrm{tx,eq}} = \mathrm{EIRP_D} + 30 + 10\log_{10}\left(\frac{B_{\mathrm{DL}}}{1\ \mathrm{MHz}}\right) - \left(L_{\mathrm{atm}} + L_{\mathrm{scin}} + L_{\mathrm{pol}} + L_{\mathrm{sh}}\right) - \Delta F \quad [\mathrm{dBm}], \tag{11}$$

where $\mathrm{EIRP_D}$ is the EIRP density in dBW/MHz, the bracketed term collects the deterministic losses that are included in the analytical link budget but not in the waveform model, and $\Delta F = 1$ dB accounts for the lower receiver noise figure of the waveform model (6 dB) relative to the link budget (7 dB). For LEO-600 with Set 2, $\mathrm{EIRP_D} = 28$ dBW/MHz (58 dBm/MHz) corresponds to 50.6 dBm per 180-kHz carrier and to $P_{\mathrm{tx,eq}} \approx 41.2$ dBm. At this value, the waveform-level SNR over 180 kHz equals the analytical downlink CNR at 50° (approximately 0.48 dB), which allows the link margins of Section 5.2 to be read directly on the power axis of the waveform-level results in Section 5.4.

The analytical and waveform-level configurations are summarized in Table 4.

Table 4. Analytical link-budget and waveform-level simulation parameters.

Parameter	LEO-600	LEO-1200	MEO-10,000	GEO-35,786
Orbit-specific parameters				
Satellite altitude, h (km)	600	1200	10,000	35,786
3GPP parameter set	Set 2	Set 2	Set 5	Set 2
Downlink satellite EIRP density (dBW/MHz)	28.0	34.0	45.4	53.5
Uplink satellite receiver G/T (dB/K)	–4.9	–4.9	3.8	14.0
Common link-budget parameters				
Geometry	Spherical Earth, $R_{\mathrm{E}} = 6371$ km; $\varepsilon_{\mathrm{u}} = 10° : 1° : 90°$; $\varepsilon_{\mathrm{g}} = \varepsilon_{\mathrm{u}}$; stationary sea-level gateway			
Carrier and bandwidth	$f_{\mathrm{UL}} = f_{\mathrm{DL}} = 2$ GHz; $B_{\mathrm{UL}} = B_{\mathrm{DL}} = 180$ kHz			
UE RF configuration	Power class 3; $P_{\mathrm{tx}} = 23$ dBm; $G_{\mathrm{tx}} = G_{\mathrm{rx}} = 0$ dBi; receiver noise figure = 7 dB; antenna temperature = 290 K			
Deterministic losses	$L_{\mathrm{atm}} = 0.2$ dB; $L_{\mathrm{scin}} = 2.2$ dB; $L_{\mathrm{pol}} = 3$ dB; $L_{\mathrm{sh}} = 3$ dB; $L_{\mathrm{cl}} = L_{\mathrm{add}} = 0$ dB			
Reference configuration	QPSK; $E_{\mathrm{b}}/N_0 = 10.5$ dB; $N_{\mathrm{Rep}} = 1$; $\gamma_{\mathrm{req,UL}} = 9.32$ dB; $\gamma_{\mathrm{req,DL}} = 0.29$ dB			
Waveform-level NPDSCH configuration				
Waveform scenario	LEO-600 downlink; $f = 2$ GHz; $\varepsilon_{\mathrm{u}} = 50°$; free-space path loss enabled			
NPDSCH configuration	QPSK; MCS 0; TBS = 208 bits; $N_{\mathrm{SF}} = 8$; $N_{\mathrm{Rep}} \in \{1, 8, 32\}$			
Channel and receiver	Rician fading; $K = 10$ dB; diffuse-component maximum Doppler $f_{\mathrm{m}} \approx 5.6$ Hz (reference-model speed setting of 3 km/h; the gateway itself is stationary); receiver noise figure = 6 dB; antenna temperature = 290 K			
Doppler configuration	Satellite Doppler included (approximately 29.6 kHz at 50°); transmitter pre-compensation enabled (ideal; zero residual common Doppler); receiver compensation disabled			
Waveform sweep	Configured transmit power P_{tx} (satellite EIRP per 180-kHz NB-IoT carrier) = 22 : 1 : 46 dBm; Set 2-equivalent operating point $P_{\mathrm{tx,eq}} \approx 41.2$ dBm (Equation (11)); 1000 transport blocks per power–repetition point; CRC-based transport-block success rate			

The reported geometry metrics comprise slant range, one-way satellite-induced propagation delay, and propagation RTT. Deterministic link-level performance is characterized by FSPL, uplink and downlink CNR, and the corresponding link margins. The representative waveform experiment evaluates NPDSCH transport-block success as a function of configured transmit power and repetition count. These complementary metrics form the basis of the results presented in Section 5.

5. Results and Discussion

5.1. Propagation-Delay Characteristics Across Orbital Scenarios

Figure 4 presents the one-way propagation delay introduced by the transparent satellite path for the four evaluated orbital scenarios. The reported value includes both the service-link and feeder-link propagation components under the symmetric-geometry assumption described in Section 4.1. In all scenarios, the delay decreases as the elevation angle increases because the corresponding ground-to-satellite slant ranges become shorter. However, the magnitude of this reduction depends strongly on orbital altitude.

For LEO-600, the one-way propagation delay decreases from approximately 12.89 ms at 10° elevation to 5.08 ms at 50° and 4.00 ms at 90°. The corresponding values for LEO-1200 are 20.89, 9.92, and 8.01 ms, respectively. The higher-altitude cases exhibit substantially larger delays: MEO-10,000 produces approximately 93.50 ms at 10°, 73.18 ms at 50°, and 66.71 ms at 90°, whereas the GEO-35,786 delay decreases from 270.73 to 238.74 ms over the same elevation interval. At the representative 50° elevation, these values correspond to propagation RTTs of approximately 10.15, 19.85, 146.37, and 494.70 ms for LEO-600, LEO-1200, MEO-10,000, and GEO-35,786, respectively.

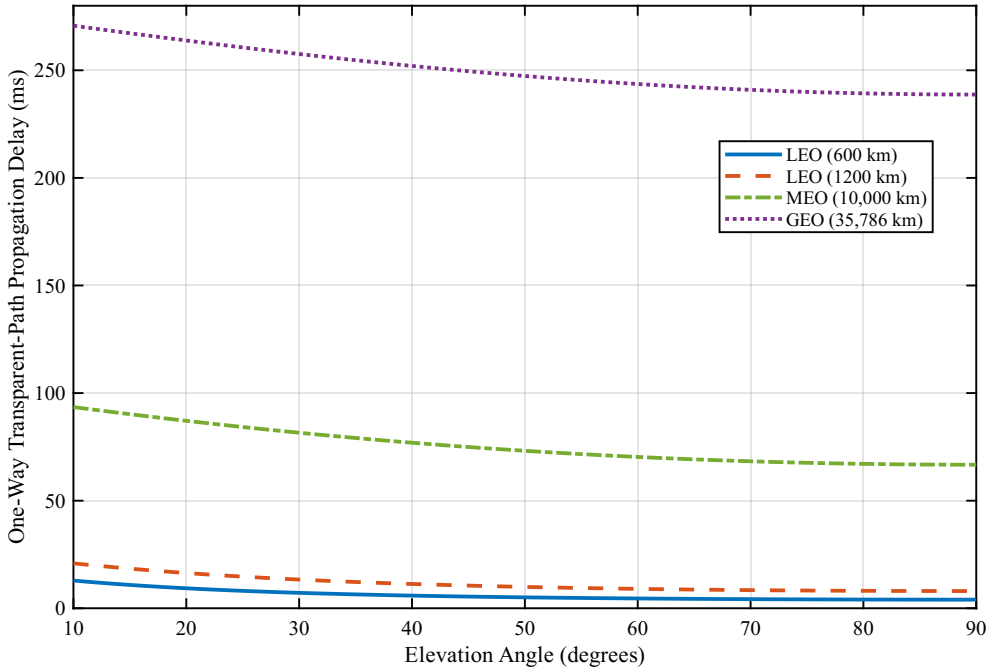


Figure 4. One-way transparent-path propagation delay versus elevation angle for the evaluated LEO, MEO, and GEO scenarios. The plotted delay includes the service- and feeder-link propagation paths and excludes scheduling, processing, queuing, and terrestrial-network delays.

For delay-tolerant periodic and historical telemetry, none of the evaluated orbits can be excluded on the basis of propagation delay alone; practical operation additionally depends on radio-link closure and higher-layer delays. Alarm and maintenance telemetry, as well as interactive supervisory commands, benefit more directly from the lower propagation delay of the LEO cases. Nevertheless, the values in Figure 4 do not represent complete end-to-end latency. NB-IoT scheduling, repetitions, retransmissions, processing, queuing, and terrestrial transport would increase the application-level delay; these contributions are quantified in Section 5.5. Time-critical protection and emergency-shutdown functions should, therefore, remain assigned to local controllers rather than to the satellite communication path.

5.2. Uplink and Downlink Link-Margin Results

Figure 5 shows the deterministic uplink and downlink margins obtained with $N_{\mathrm{Rep}} = 1$ over the evaluated 180-kHz channel configuration. A positive margin indicates that the corresponding direction satisfies its analytical reference CNR requirement without additional repetitions, whereas a negative margin identifies the remaining coverage deficit. The zero-margin boundary is included in both panels to make the link-closure regions explicit.

The uplink is the limiting direction in all four reference scenarios. For LEO-600, the uplink margin improves from approximately −17.76 dB at 10° to −9.67 dB at 50° and −7.60 dB at 90°. LEO-1200 follows the same elevation-dependent trend but remains between approximately −21.95 and −13.62 dB. The uplink margins of MEO-10,000 and GEO-35,786 remain below −23 dB throughout the evaluated angular range. Consequently, none of the scenarios provides uplink closure with a single transmission under the adopted terminal, bandwidth, and loss assumptions. The improvement obtained at higher elevation is most pronounced for the LEO cases because their slant ranges vary more strongly with elevation angle.

The downlink results are less restrictive for the LEO configurations. The LEO-600 margin increases from approximately −7.90 dB at 10° to 0.19 dB at 50° and 2.26 dB at 90°, crossing the zero-margin boundary at approximately 49°. LEO-1200 achieves downlink closure at approximately 47°, with a margin increasing from −6.09 dB at 10° to 2.24 dB at 90°. Its slightly earlier crossing does not indicate that greater altitude is intrinsically beneficial; it results from the higher satellite EIRP density assigned to the LEO-1200 reference configuration. MEO-10,000 and GEO-35,786 remain below the zero-margin boundary even at 90°, where their downlink margins are approximately −4.78 and −7.76 dB, respectively.

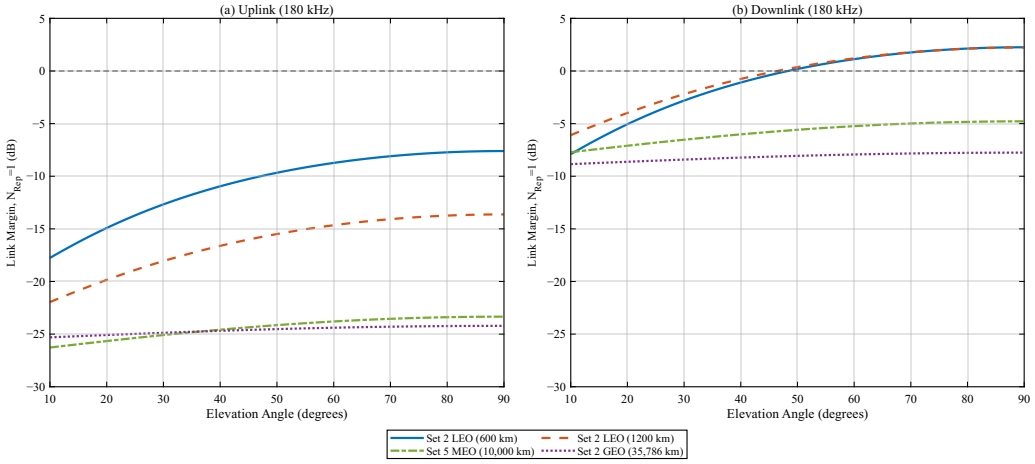


Figure 5. Deterministic NB-IoT link margin with $N_{\mathrm{Rep}} = 1$: (**a**) uplink and (**b**) downlink. The dashed horizontal line denotes the zero-margin link-closure boundary.

Operational connectivity requires both directions to be supported. For example, at 50°, the LEO-600 downlink has a small positive margin of 0.19 dB, while its uplink still has a deficit of approximately 9.67 dB. Downlink closure alone is, therefore, insufficient for supervisory operation, which requires both command delivery and return telemetry. The results identify uplink coverage enhancement, through repetition or an improved terminal antenna configuration, as the primary requirement; the corresponding coverage-enhancement gain is quantified in Section 5.3. They also show that performance cannot be attributed to altitude alone: orbit-specific EIRP density, receiver G/T, and propagation distance jointly determine the margin. In particular, MEO-10,000 uses 3GPP Set 5, whereas the remaining cases use Set 2; hence, the MEO result represents a comparison between different reference configurations rather than an identical-payload orbit comparison.

5.3. Elevation-Dependent Shadowing, Pass-Level Outage, and Required Coverage-Enhancement Gain

The sensitivity of the crossing angles to the loss assumptions is examined next. Because Equations (5)–(7) are linear in decibels, a change ΔL in any loss term shifts the margin curves in Figure 5 by $-\Delta L$, and the crossing angle moves according to the local slope of the curve. Near the zero crossing, the downlink margin increases by approximately 0.11 dB per degree for LEO-600 and 0.10 dB per degree for LEO-1200. Consequently, a $\pm$1-dB change in the total loss moves the LEO-600 crossing (48.3°, i.e., approximately 49° on the 1° grid) to approximately 58° and 41°, respectively, and the LEO-1200 crossing (46.4°, i.e., approximately 47°) to approximately 57° and 38°. When the fixed 3-dB shadow margin is replaced by the elevation-dependent 95th-percentile margin $1.645\,\sigma_{\mathrm{SF}}(\varepsilon)$ of TR 38.811 (Section 4.2), the crossing angles decrease to approximately 38° for LEO-600 and 36° for LEO-1200. The crossing angles reported in Section 5.2 are, therefore, conservative. The uplink conclusion is unaffected, because the largest reduction of the shadow margin obtained with the elevation-dependent model is $3 - 1.645 \times 0.72 \approx 1.8$ dB, which is much smaller than the uplink deficits of 7.6–26.3 dB.

The pass-level outage probability is evaluated next. Table 5 reports the outage probability obtained from Equations (8)–(10) for single transmission ($G_{\mathrm{CE}} = 0$), both for an overhead pass and averaged over passes with uniformly distributed ground-track offsets, together with the coverage-enhancement gain required to reduce the pass-averaged outage probability to 10% and 1%. For GEO, a fixed elevation of 50° is used. The visibility duration of an overhead pass above 10° is approximately 8.5, 14.6, and 111 min for LEO-600, LEO-1200, and MEO-10,000, respectively.

Table 5. Pass-level outage probability and required coverage-enhancement gain derived from the margin–elevation curves with the elevation-dependent rural-LOS shadowing of TR 38.811 ($\varepsilon_{\min} = 10°$; GEO evaluated at 50°).

Scenario	Link	P_{out}, Overhead Pass, $N_{\mathrm{Rep}} = 1$ (%)	$\bar{P}_{\mathrm{out}}$, Pass-Averaged, $N_{\mathrm{Rep}} = 1$ (%)	G_{CE} for $\bar{P}_{\mathrm{out}} \leq 10\%$ (dB)	G_{CE} for $\bar{P}_{\mathrm{out}} \leq 1\%$ (dB)	Ideal-Gain Lower Bound on N_{Rep} for 1%
LEO-600	DL	49.2	73.2	5.2	7.4	6
	UL	100	100	15.0	17.3	54
LEO-1200	DL	35.2	56.3	3.4	5.6	4
	UL	100	100	19.2	21.5	141
MEO-10,000	DL	98.6	99.0	5.4	7.3	6
	UL	100	100	24.0	25.8	383
GEO-35,786	DL	>99.9 (fixed elevation)		6.9	8.4	7
	UL	100 (fixed elevation)		23.3	24.8	304

Three observations follow from Table 5. First, without coverage enhancement, the uplink is in outage during the entire pass in all scenarios, whereas the LEO downlinks are available during the high-elevation part of the pass; the pass-averaged downlink outage exceeds the overhead-pass value because passes with larger ground-track offsets do not reach the crossing elevation. Second, the downlink requirements are moderate: the LEO-600 downlink requires 5.2 and 7.4 dB for 10% and 1% outage, respectively, which is within the realized NPDSCH repetition gains of approximately 5.5 dB for $N_{\mathrm{Rep}} = 8$ and 9 dB for $N_{\mathrm{Rep}} = 32$ observed in Section 5.4. Third, the uplink requires 15.0–17.3 dB for LEO-600, 19.2–21.5 dB for LEO-1200, and approximately 23–26 dB for the MEO and GEO reference cases. Even under ideal accumulation, a 1% pass-averaged outage, therefore, requires at least 54 NPUSCH repetitions for LEO-600 (i.e., 64 in the standardized set of 1 to 128 repetitions [47]), more than the maximum of 128 repetitions for LEO-1200, and approximately

300–400 repetitions for MEO and GEO. Because realized repetition gains are below the ideal gains, these values are lower bounds. The uplink deficit can, therefore, not be closed by NPUSCH repetition alone in the higher-orbit cases and requires additional measures, such as longer single-tone resource units or a higher-gain terminal antenna. This quantifies the conclusion of Section 5.2 that uplink coverage enhancement is the primary requirement. The outage values refer to a single satellite link and do not include constellation-level availability or handover; with overlapping coverage, the gateway can additionally select the satellite with the highest elevation angle.

5.4. Waveform-Level NPDSCH Reliability and Repetition Gain

A waveform-level evaluation was conducted to examine how NPDSCH repetitions affect transport-block reliability at a representative operating point. The selected case uses LEO-600 at 2 GHz and 50° elevation, for which the slant range and free-space path loss are approximately 760.823 km and 156.094 dB, respectively. A 208-bit transport block is transmitted using QPSK, MCS 0, and eight NPDSCH subframes over a Rician fading channel with a 10-dB K-factor. The sweep evaluates $N_{\mathrm{Rep}} \in \{1, 8, 32\}$ from 22 to 46 dBm in 1-dB increments, using 1000 decoded transport blocks per power point. These repetition counts are selected as sensitivity cases and do not represent operating requirements derived from the deterministic link-margin deficits. Transport-block success is determined from the CRC outcome after NPDSCH channel estimation, soft combining, and decoding.

As shown in Figure 6, increasing the repetition count shifts the transport-block reliability transition toward a lower configured transmit power. With $N_{\mathrm{Rep}} = 1$, the curve enters its main transition region only at the higher end of the evaluated power range, and near-complete transport-block recovery is reached at approximately 42–44 dBm. For $N_{\mathrm{Rep}} = 8$, the corresponding transition occurs at approximately 34–38 dBm, while $N_{\mathrm{Rep}} = 32$ enters the high-success region at approximately 30–34 dBm. At 38 dBm, the $N_{\mathrm{Rep}} = 8$ and $N_{\mathrm{Rep}} = 32$ configurations are close to saturation, whereas the single-transmission configuration remains within its transition region. The results demonstrate the reliability improvement provided by repetition under the selected Rician fading conditions. Measured at the 50% success point, the curves are located at approximately 37.7, 32.2, and 28.8 dBm for $N_{\mathrm{Rep}} = 1$, 8, and 32, respectively, which corresponds to realized repetition gains of approximately 5.5 and 9 dB. These gains are lower than the ideal energy-accumulation gains of $10 \log_{10} 8 = 9.0$ dB and $10 \log_{10} 32 = 15.1$ dB because channel estimation, fading, and synchronization do not improve proportionally with the number of repetitions. This observation supports the decision not to apply an ideal accumulation gain in the deterministic link budget (Section 4.2).

The repetition count represents the number of physical-layer transmissions of the same NPDSCH transport block and should not be interpreted as a throughput-neutral reliability improvement. Higher N_{Rep} increases the observation energy available to the decoder but also occupies additional downlink resources and extends the transport-block transmission duration. Repetition, therefore, introduces a trade-off among reliability, resource consumption, and transmission time. Moreover, because Figure 6 evaluates the satellite-to-terminal downlink, it does not quantify the battery lifetime of the remote gateway or demonstrate that the uplink deficits identified in Figure 5 have been eliminated.

Figures 5 and 6 provide complementary rather than interchangeable evaluations. Figure 5 evaluates whether the analytical reference link budget closes under the adopted orbit-specific EIRP-density and G/T parameters. In contrast, Figure 6 varies the configured transmit power for one selected LEO downlink and includes Rician fading, Doppler effects, reference-signal-based channel estimation, soft combining, and CRC-based decoding. The two figures are nevertheless linked through Equation (11): the Set 2 LEO-600 satellite EIRP

density corresponds to $P_{\mathrm{tx,eq}} \approx 41.2$ dBm on the horizontal axis of Figure 6. At this point, the $N_{\mathrm{Rep}} = 1$ curve lies in its upper transition region, with a transport-block success rate of approximately 90%, which is consistent with the small analytical downlink margin of 0.19 dB at 50°. With $N_{\mathrm{Rep}} = 8$ and 32, the same operating point lies approximately 9 and 12 dB above the respective 50% points and provides practically error-free decoding. The waveform results, therefore, quantify how much of the fading and implementation margin that is not captured by the deterministic link budget can be recovered through NPDSCH repetitions.

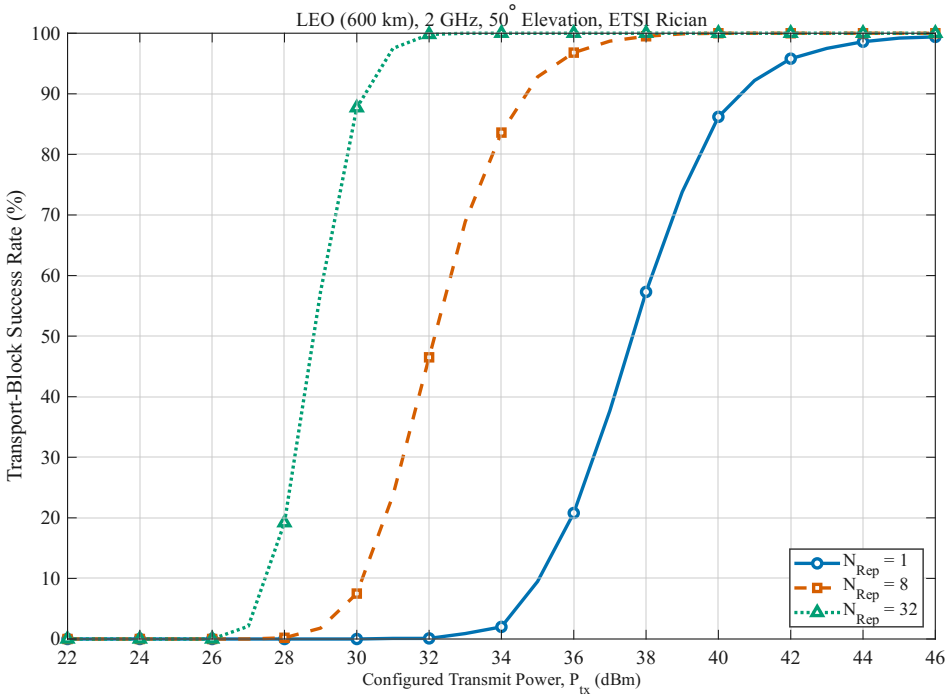


Figure 6. Waveform-level NPDSCH transport-block success rate for the representative LEO-600 downlink at 2 GHz and 50° elevation over a Rician fading channel with a 10-dB K-factor, for $N_{\mathrm{Rep}} \in \{1, 8, 32\}$. The transmit power on the horizontal axis is the configured transmit power P_{tx}, i.e., the satellite EIRP per 180-kHz NB-IoT carrier (Equation (11)); the Set 2-equivalent LEO-600 operating point is $P_{\mathrm{tx,eq}} \approx 41.2$ dBm.

The waveform-level validation was restricted to the downlink for two reasons. First, the link-closure decision for both directions is already made by the analytical link budget in Figure 5, which identifies the uplink as the limiting direction. The purpose of the waveform experiment is different: it quantifies, at one representative operating point, how far the realized repetition gain under fading, Doppler, and practical channel estimation falls below the ideal accumulation gain, and it thereby supports the decision not to apply an ideal repetition gain in the deterministic link budget. Second, a credible NPUSCH NTN waveform model requires the Release 17 UE-side mechanisms, namely GNSS-based timing-advance and frequency pre-compensation using the broadcast satellite ephemeris, together with their residual errors [15]. These residual errors depend on GNSS accuracy, ephemeris age, and implementation-specific validity timers, for which TR 36.763 provides no calibrated reference values; assuming such values would add uncertainty rather than insight at the present level of analysis. Because the uplink also differs from the downlink in its waveform, reference signals, and resource allocation, the downlink repetition gains in Figure 6 are not transferred quantitatively to the uplink; they only indicate that uplink repetition levels should not be dimensioned on the basis of ideal accumulation gains. A waveform-level NPUSCH evaluation including UE-side pre-compensation errors is, therefore, identified as future work.

The conclusion that uplink coverage enhancement is the primary requirement does not rely on the downlink waveform result; it follows from three observations that jointly bound the uplink behavior without requiring an uplink waveform model. First, the pass-level analysis in Table 5 shows that, even under ideal accumulation, the LEO-600 uplink requires 15.0–17.3 dB of coverage-enhancement gain, i.e., approximately 32–54 repetitions, compared with 5.2–7.4 dB for the downlink. Second, the waveform result provides an empirical calibration of the analytical threshold: at the Set 2 operating point, where the analytical downlink margin is 0.19 dB, the single-transmission success rate is approximately 90%, and the 50% point lies approximately 3.5 dB lower, i.e., at an analytical margin of approximately -3.3 dB. Even if the NPUSCH receiver attained the same favorable offset relative to its analytical threshold, which is not assumed elsewhere in this study, the LEO-600 uplink at 50°, with a margin of -9.67 dB, would remain approximately 6.4 dB below its 50% success point and would, therefore, be practically in outage without repetition. Third, any realized uplink repetition gain below the ideal accumulation gain, as observed for NPDSCH, can only increase the required number of repetitions. Consequently, an uplink BLER sweep at 50° would determine how many repetitions beyond the lower bounds of Table 5 are required, but it could not reverse the identification of the uplink as the limiting direction.

5.5. Latency Impact of Repetition, Random Access, and Timing Advance

The propagation delays in Figure 4 are only one component of the latency experienced by a SCADA supervisory loop. With coverage enhancement, the air-interface transmission time can exceed the propagation delay, particularly in LEO. Because each NPDSCH transport block in the adopted configuration occupies $N_{\mathrm{SF}} = 8$ subframes, its minimum downlink air time is $8N_{\mathrm{Rep}}$ ms, i.e., 8, 64, and 256 ms for $N_{\mathrm{Rep}} = 1$, 8, and 32, rather than N_{Rep} ms. On the uplink, an NPUSCH resource unit lasts $T_{\mathrm{RU}} = 1$, 2, 4, 8, or 32 ms for 12-tone, 6-tone, 3-tone, 15-kHz single-tone, and 3.75-kHz single-tone allocations, respectively [49]. In Release 17 IoT-NTN, the UE applies a timing advance that pre-compensates the full service- and feeder-link round trip using its GNSS position, the broadcast ephemeris, and broadcast common timing-advance parameters, and the scheduling offset K_{offset} between an uplink grant and the corresponding NPUSCH transmission is extended accordingly [15]. Consequently, for a terminal in connected mode, the lower bound of a command–response loop observed at the eNB is

$$T_{\mathrm{loop}} \gtrsim N_{\mathrm{SF}} N_{\mathrm{Rep}}^{\mathrm{DL}} T_{\mathrm{SF}} + N_{\mathrm{RU}} N_{\mathrm{Rep}}^{\mathrm{UL}} T_{\mathrm{RU}} + \mathrm{RTT}_{\mathrm{prop}} + T_{\mathrm{proc}}, \tag{12}$$

where $T_{\mathrm{SF}} = 1$ ms and T_{proc} collects NPDCCH scheduling, processing, and terrestrial transport delays. If the gateway is in idle mode, a random-access procedure is required first. Its minimum duration is

$$T_{\mathrm{RA}} \gtrsim N_{\mathrm{Rep}}^{\mathrm{PRACH}} T_{\mathrm{PRACH}} + 2\,\mathrm{RTT}_{\mathrm{prop}}, \tag{13}$$

where $T_{\mathrm{PRACH}} = 5.6$ ms for NPRACH preamble format 0 [49], and the two round trips correspond to the preamble–response and connection-request–contention-resolution exchanges. Table 6 evaluates Equations (12) and (13) at 50° elevation with $N_{\mathrm{RU}} = 1$, $T_{\mathrm{proc}} = 0$, and equal repetition counts in all channels. The values are lower bounds because subframes carrying NPSS, NSSS, NPBCH, and system information are not available for NPDSCH, and because NPDCCH repetitions, HARQ feedback, and core-network delays are excluded.

Table 6. Indicative lower bounds of air-interface latency at 50° elevation (ms), obtained from Equations (12) and (13).

Component\N_{Rep}	LEO-600 (RTT_{prop} = 10.15 ms)			GEO-35,786 (RTT_{prop} = 494.70 ms)		
	1	8	32	1	8	32
NPDSCH air time ($N_{SF} = 8$)	8	64	256	8	64	256
Command–response loop, 12-tone NPUSCH	19.2	82.2	298.2	503.7	566.7	782.7
Command–response loop, 15-kHz single-tone NPUSCH	26.2	138.2	522.2	510.7	622.7	1006.7
Additional random access from idle mode	25.9	65.1	199.5	995.0	1034.2	1168.6

Three conclusions follow from Table 6. First, in LEO, repetition rather than propagation dominates latency: at $N_{Rep} = 32$, the NPDSCH air time alone (256 ms) is approximately 50 times the one-way LEO-600 propagation delay and even exceeds the GEO one-way propagation delay. Second, LEO command–response loops remain below the 500 ms operator-command reference (TT2 in Table 1) for $N_{Rep} \leq 8$, and also for $N_{Rep} = 32$ with multi-tone uplink, whereas all GEO loops exceed this reference because the propagation RTT alone is approximately 495 ms. Third, when the gateway must first perform random access from idle mode, approximately 26–200 ms is added in LEO and approximately 1.0–1.2 s in GEO; with power-saving mode or long extended-DRX cycles, the terminal may additionally be unreachable for downlink commands until its next wake-up [34]. Since the edge gateway at an energy site is typically supplied by the site's own auxiliary power, it can remain in connected mode or use short DRX cycles when supervisory control is required. These latencies are compatible with periodic monitoring (TT0) in all orbits and with alarm delivery (TT1) and non-time-critical supervisory commands in LEO, but they confirm that SCADA protocol timers must be configured for second-level response times and that protection functions (TT5–TT6) must remain local.

5.6. Cost–Benefit Considerations

The economic case for NTN connectivity depends on the alternatives available at a given site. Terrestrial options, such as fiber, microwave relay, and cellular extension, offer high capacity and low latency, but their deployment cost grows with distance and terrain and is often prohibitive for isolated or offshore sites [7], and the associated CAPEX and OPEX leave remote areas uncovered [8]. In contrast, the NB-IoT NTN terminal considered here is a 3GPP power-class-3 device with 23-dBm transmit power and a 0-dBi omnidirectional antenna (Table 4) [15]; it requires neither antenna pointing nor a dedicated high-power satellite terminal, and its cost is largely independent of the site location. A technical cost driver that can be quantified from the present study is the satellite radio-resource occupation per delivered message. The traffic classes in Table 1 require only 10–500 bytes per message, i.e., one to 20 transport blocks of 208 bits, but each transport block occupies $8N_{Rep}$ ms of NPDSCH air time (Section 5.5), and uplink resources grow in the same way with the NPUSCH repetition count. Even under ideal accumulation, closing the single-transmission uplink deficit of 9.67 dB for LEO-600 at 50° requires approximately ten repetitions, whereas the deficits of more than 23 dB for MEO-10,000 and GEO-35,786 would require more than 200. Consequently, under the adopted terminal configuration, the resource consumption and, thus, the radio-resource occupation required per delivered message is lower for the evaluated LEO case than for the higher-orbit reference cases. Whether this translates into a lower monetary operating cost depends on the satellite operator's tariff, scheduling, and service model.

On the benefit side, the value of NTN connectivity arises mainly from avoided losses rather than from the communication service itself. SCADA-based condition monitoring

enables earlier fault detection and optimized maintenance, which reduces operating costs and generation losses [27]; remote diagnosis reduces the number of site visits to inaccessible locations; and a backup path preserves the visibility of the site when terrestrial links fail during natural disasters [9]. NTN connectivity is, therefore, economically preferable when its discounted capital and operating costs, net of these avoided losses, are lower than those of the best available alternative. Because terrestrial costs increase with the distance to the nearest network, whereas the NTN terminal cost does not, this condition is most likely to be satisfied for remote, offshore, and widely distributed assets; where terrestrial coverage already exists, the benefit of NTNs lies primarily in its resilience value as a backup link. A quantitative, site-specific evaluation requires tariff, installation, and generation-loss data and is left for future work.

5.7. Application Implications and Scope Limitations

The combined results have different implications for the three traffic classes defined in Section 3.3. Periodic monitoring is comparatively tolerant of propagation delay and repetition-induced transmission time, making it the least restrictive category. Alarm and predictive-maintenance telemetry require improved reliability and shorter delivery time and, therefore, benefit from the lower propagation delay of the LEO cases. Supervisory control is more restrictive because a successful downlink command must be accompanied by a reliable uplink status response. The negative single-transmission uplink margins show that this function requires explicit uplink coverage enhancement and cannot be justified from the downlink reliability result alone.

No evaluated orbit can be identified as universally superior from these results. LEO provides a clear propagation-delay advantage and, in the selected waveform case, supports high NPDSCH reliability when sufficient power or repetition is available. Nevertheless, the link-budget comparison also depends on orbit-specific satellite EIRP density and receiver G/T. The MEO case additionally belongs to a different 3GPP parameter set, while GEO exhibits relatively weak elevation dependence but substantially greater propagation delay. Orbit selection must, therefore, consider the traffic class, available satellite and terminal link budget, permissible repetition overhead, and service-availability requirements together.

Finally, the evaluation represents a fixed remote-energy gateway under the adopted rural outdoor, transparent-payload, S-band, and sufficient feeder-link margin assumptions. Figure 4 does not include constellation availability or handover, and Figure 5 uses deterministic losses and fixed margin assumptions, whose conservativeness is verified with the elevation-dependent shadowing model in Section 5.3. The waveform analysis is restricted to one LEO-600 downlink operating point and does not constitute an orbit-wide outage analysis; the pass-level outage in Table 5 is derived analytically for a single satellite link, a non-rotating Earth, and log-normal shadowing, and it excludes fast fading, which is addressed only at the waveform level. Random-access congestion, higher-layer retransmissions, scheduling delay, routing, queuing, detailed feeder-link performance, power-amplifier nonlinearity, terminal battery lifetime, and a quantitative, site-specific system-level CAPEX/OPEX evaluation remain outside the present scope. Within these boundaries, the results identify the link-budget and delay conditions under which NTN-assisted monitoring, alarm delivery, and non-time-critical supervisory communication may be supported. They also confirm that time-critical protection and emergency-shutdown loops should remain local to the renewable-energy site.

6. Conclusions

This study proposed a four-layer, 3GPP Release 17-aligned architecture for extending IoT connectivity to remote green-energy facilities beyond reliable terrestrial coverage and evaluated its communication characteristics. The architecture integrates local sensor aggregation and edge processing with NB-IoT access through a transparent satellite payload, terrestrial E-UTRAN/EPC functions, and centralized IoT and EMS/SCADA applications. A 3GPP-aligned analytical framework was developed to quantify satellite geometry, transparent-path propagation delay, and deterministic uplink and downlink link margins for LEO-600, LEO-1200, MEO-10,000, and GEO-35,786 scenarios. This analysis was complemented by a waveform-level NPDSCH reliability experiment for a representative LEO-600 downlink.

The results showed that orbital altitude and elevation angle strongly affect propagation delay. At an elevation angle of 50°, the one-way satellite-induced propagation delays were approximately 5.08, 9.92, 73.18, and 247.35 ms for LEO-600, LEO-1200, MEO-10,000, and GEO-35,786, respectively. However, link feasibility was not determined by altitude alone because orbit-specific EIRP density, receiver G/T, propagation distance, and terminal configuration jointly influenced the available margin. With $N_{\mathrm{Rep}} = 1$, the uplink remained the limiting direction in all evaluated scenarios. The LEO-600 and LEO-1200 downlinks achieved link closure above approximately 49° and 47°, respectively, whereas their uplinks still required coverage enhancement. The waveform-level results further demonstrated that increasing the selected NPDSCH repetition count from 1 to 8 or 32 shifted the transport-block reliability transition toward lower configured transmit-power values. These repetition counts were evaluated as sensitivity cases and were not derived as deterministic requirements from the link-margin deficits. A pass-level analysis with the elevation-dependent shadowing of TR 38.811 showed that the fixed-loss crossing angles are conservative and that, for a pass-averaged outage probability of 1%, the LEO-600 downlink requires approximately 7.4 dB of coverage-enhancement gain, which is within the realized gain of 32 NPDSCH repetitions, whereas the uplink requires approximately 17.3 dB, corresponding to at least 54 NPUSCH repetitions under ideal accumulation, and the MEO and GEO uplinks exceed the maximum NPUSCH repetition gain. The associated reliability improvement is accompanied by increased resource occupation and transmission duration and should, therefore, be treated as a reliability–efficiency trade-off. The realized repetition gains of approximately 5.5 and 9 dB for eight and 32 repetitions remained below the ideal accumulation gains, and the configured transmit power was mapped explicitly to the 3GPP satellite EIRP density, which placed the Set 2 LEO-600 operating point in the upper transition region of the single-transmission curve. The latency analysis further showed that, in LEO, repetition rather than propagation dominates the air-interface latency, whereas in GEO the propagation RTT alone approaches the 500 ms operator-command reference.

From an application perspective, none of the evaluated orbital categories can be excluded for delay-tolerant periodic monitoring on the basis of propagation delay alone; practical support additionally requires adequate radio-link closure. Alarm and predictive-maintenance traffic benefit more directly from the lower propagation delay of LEO systems, while bidirectional supervisory control additionally requires reliable uplink coverage through repetition, improved terminal antenna performance, or other coverage-enhancement mechanisms. Time-critical protection and emergency-shutdown functions should remain local to the renewable-energy facility. Consequently, no orbit can be regarded as universally optimal; orbit and system configuration should instead be selected jointly according to the traffic class, link budget, permissible repetition overhead, and service-availability requirements.

The findings are subject to the adopted fixed outdoor-gateway, rural line-of-sight, S-band, transparent-payload, and sufficient feeder-link margin assumptions. Future work should examine constellation-level availability and handover, extend the waveform-level evaluation to uplink transmission with UE-side timing and frequency pre-compensation errors and to downlink reception with residual Doppler and receiver-side frequency tracking, quantify the site-specific cost–benefit ratio, and validate the proposed framework through representative field deployments.

Author Contributions: Conceptualization, K.Z.; methodology, K.Z. and S.K.; software, validation, formal analysis, data curation, and visualization, K.Z. and S.K.; investigation, K.Z. and S.K.; writing—original draft preparation, K.Z. and S.K.; writing—review and editing, K.Z., S.K., and M.Y.; supervision, M.Y. All authors have read and agreed to the published version of the manuscript.

Funding: This research was funded by the Scientific and Technological Research Council of Türkiye (TÜBİTAK) through the 1515 Frontier Research and Development Laboratories Support Program for the Türk Telekom 6G Research and Development Laboratory, grant number 5249902.

Data Availability Statement: The numerical data generated and analyzed in this study were obtained from the MATLAB simulations described in the article. The data supporting the reported findings are presented within the article. Additional simulation outputs are available from the corresponding author upon reasonable request.

Acknowledgments: This research was supported by Türk Telekom within the scope of the project titled "Development of Hybrid Wireless Communication Technologies for Beyond 5G Communication Systems". During the preparation of this manuscript, the authors used large language models for the purposes of language polishing. The authors have reviewed and edited the output and take full responsibility for the content of this publication.

Conflicts of Interest: Authors Kahraman Zaim and Seyit Karatepe are employed by the company Türk Telekomünikasyon AŞ. Author Murat Yücel is employed by the company YIMI Electronics & Communication Co. The authors declare that the research was conducted in the absence of any other commercial or financial relationships that could be construed as a potential conflict of interest. The authors declare that this study received funding from the Scientific and Technological Research Council of Türkiye (TÜBİTAK) through the 1515 Frontier Research and Development Laboratories Support Program for the Türk Telekom 6G Research and Development Laboratory (grant number 5249902). The funder was not involved in the study design, collection, analysis, interpretation of data, the writing of this article or the decision to submit it for publication.

Abbreviations

The following abbreviations are used in this manuscript:

3GPP	Third Generation Partnership Project
CAPEX	Capital expenditure
CINR	Carrier-to-interference-plus-noise ratio
CNR	Carrier-to-noise ratio
CoAP	Constrained Application Protocol
CRC	Cyclic redundancy check
DL	Downlink
DRX	Discontinuous reception
EIRP	Effective isotropic radiated power
EMS	Energy Management System
eMTC	Enhanced Machine-Type Communication
eNB	Evolved Node B
EPC	Evolved Packet Core
E-UTRAN	Evolved Universal Terrestrial Radio Access Network

FSPL	Free-space path loss
G/T	Gain-to-noise-temperature ratio
GEO	Geostationary Earth orbit
GNSS	Global navigation satellite system
HARQ	Hybrid automatic repeat request
IEC	International Electrotechnical Commission
IoT	Internet of Things
LEO	Low Earth Orbit
LOS	Line of sight
LTE-M	Long-Term Evolution for Machines
MCS	Modulation and coding scheme
MEO	Medium Earth orbit
MQTT	Message Queuing Telemetry Transport
NB-IoT	Narrowband Internet of Things
NPBCH	Narrowband Physical Broadcast Channel
NPDCCH	Narrowband Physical Downlink Control Channel
NPDSCH	Narrowband Physical Downlink Shared Channel
NPRACH	Narrowband Physical Random Access Channel
NPSS	Narrowband Primary Synchronization Signal
NPUSCH	Narrowband Physical Uplink Shared Channel
NR	New Radio
NRS	Narrowband Reference Signal
NSSS	Narrowband Secondary Synchronization Signal
NTN	Non-terrestrial network
OPC UA	Open Platform Communications Unified Architecture
OPEX	Operational expenditure
PV	Photovoltaic
QPSK	Quadrature phase-shift keying
RF	Radio frequency
RTT	Round-trip time
RU	Resource unit
SCADA	Supervisory Control and Data Acquisition
SNR	Signal-to-noise ratio
TBS	Transport block size
TCP	Transmission Control Protocol
TR	Technical Report
TS	Technical Specification
UE	User equipment
UL	Uplink

References

1. Dong, F.; Qin, C.; Zhang, X.; Zhao, X.; Pan, Y.; Gao, Y.; Zhu, J.; Li, Y. Towards Carbon Neutrality: The Impact of Renewable Energy Development on Carbon Emission Efficiency. *Int. J. Environ. Res. Public Health* **2021**, *18*, 13284. [CrossRef] [PubMed]
2. Roy, A.; Auger, F.; Dupriez-Robin, F.; Bourguet, S.; Tran, Q.T. Electrical Power Supply of Remote Maritime Areas: A Review of Hybrid Systems Based on Marine Renewable Energies. *Energies* **2018**, *11*, 1904. [CrossRef]
3. Norel-Wilson, L. Institute Insights: Renewable Energy in Remote Locations. The Renewable Energy Institute. Available online: https://www.renewableinstitute.org/institute-insights-renewable-energy-in-remote-locations/ (accessed on 23 September 2026).
4. Khalid, M. Smart Grids and Renewable Energy Systems: Perspectives and Grid Integration Challenges. *Energy Strategy Rev.* **2024**, *51*, 101299. [CrossRef]
5. Gharavi, H.; Ghafurian, R. Smart Grid: The Electric Energy System of the Future. *Proc. IEEE* **2011**, *99*, 917–921. [CrossRef]
6. Cheng, N.; Xu, W.; Shi, W.; Zhou, Y.; Lu, N.; Zhou, H.; Shen, X. Air-Ground Integrated Mobile Edge Networks: Architecture, Challenges, and Opportunities. *IEEE Commun. Mag.* **2018**, *56*, 26–32. [CrossRef]

7. Giordani, M.; Polese, M.; Mezzavilla, M.; Rangan, S.; Zorzi, M. Toward 6G Networks: Use Cases and Technologies. *IEEE Commun. Mag.* **2020**, *58*, 55–61. [CrossRef]
8. International Telecommunication Union. *Connecting Humanity: Assessing Investment Needs of Connecting Humanity to the Internet by 2030*; Technical Report; International Telecommunication Union: Geneva, Switzerland, 2020. Available online: https://www.itu.int/hub/publication/d-gen-invest-con-2020/ (accessed on 23 September 2026).
9. Wang, Y.; Chen, C.; Wang, J.; Baldick, R. Research on Resilience of Power Systems Under Natural Disasters—A Review. *IEEE Trans. Power Syst.* **2016**, *31*, 1604–1613. [CrossRef]
10. Gungor, V.C.; Sahin, D.; Kocak, T.; Ergut, S.; Buccella, C.; Cecati, C.; Hancke, G.P. Smart Grid Technologies: Communication Technologies and Standards. *IEEE Trans. Ind. Inform.* **2011**, *7*, 529–539. [CrossRef]
11. Katiraei, F.; Iravani, M.R. Power Management Strategies for a Microgrid With Multiple Distributed Generation Units. *IEEE Trans. Power Syst.* **2006**, *21*, 1821–1831. [CrossRef]
12. Dobson, I.; Carreras, B.A.; Lynch, V.E.; Newman, D.E. Complex Systems Analysis of Series of Blackouts: Cascading Failure, Critical Points, and Self-Organization. *Chaos Interdiscip. J. Nonlinear Sci.* **2007**, *17*, 026103. [CrossRef] [PubMed]
13. Giordani, M.; Zorzi, M. Non-Terrestrial Networks in the 6G Era: Challenges and Opportunities. *IEEE Netw.* **2021**, *35*, 244–251. [CrossRef]
14. Kodheli, O.; Lagunas, E.; Maturo, N.; Sharma, S.K.; Shankar, B.; Montoya, J.F.M.; Duncan, J.C.M.; Spano, D.; Chatzinotas, S.; Kisseleff, S.; et al. Satellite Communications in the New Space Era: A Survey and Future Challenges. *IEEE Commun. Surv. Tutor.* **2021**, *23*, 70–109. [CrossRef]
15. 3GPP. *Study on Narrow-Band Internet of Things (NB-IoT)/Enhanced Machine Type Communication (eMTC) Support for Non-Terrestrial Networks (NTN)*; Technical Report 3GPP TR 36.763 V17.0.0 (Release 17); 3rd Generation Partnership Project (3GPP): Sophia Antipolis, France, 2021.
16. 3GPP. *Study on New Radio (NR) to Support Non-Terrestrial Networks*; Technical Report 3GPP TR 38.811 V15.4.0 (Release 15); 3rd Generation Partnership Project (3GPP): Sophia Antipolis, France, 2020.
17. 3GPP. *Solutions for NR to Support Non-Terrestrial Networks (NTN)*; Technical Report 3GPP TR 38.821 V16.0.0 (Release 16); 3rd Generation Partnership Project (3GPP): Sophia Antipolis, France, 2019.
18. Conti, M.; Guidotti, A.; Amatetti, C.; Vanelli-Coralli, A. NB-IoT over Non-Terrestrial Networks: Link Budget Analysis. In Proceedings of the 2020 IEEE Global Communications Conference (GLOBECOM), Taipei, Taiwan, 7–11 December 2020; pp. 1–6. [CrossRef]
19. Kodheli, O.; Andrenacci, S.; Maturo, N.; Chatzinotas, S.; Zimmer, F. Resource Allocation Approach for Differential Doppler Reduction in NB-IoT over LEO Satellite. In Proceedings of the 2018 9th Advanced Satellite Multimedia Systems Conference and the 15th Signal Processing for Space Communications Workshop (ASMS/SPSC), Berlin, Germany, 10–12 September 2018; pp. 1–8. [CrossRef]
20. Şahin, B.; Şahin, Y. Yenilenebilir Enerji Kaynakları ve Yeşil Finans Alanında Yapılan Çalışmaların Yazın Taraması. *MAS J. Appl. Sci.* **2024**, *9*, 414–426. (In Turkish) [CrossRef]
21. Edenhofer, O.; Pichs-Madruga, R.; Sokona, Y.; Seyboth, K.; Matschoss, P.; Kadner, S.; Zwickel, T.; Eickemeier, P.; Hansen, G.; Schlömer, S.; et al. (Eds.) *Renewable Energy Sources and Climate Change Mitigation: Special Report of the Intergovernmental Panel on Climate Change*; Cambridge University Press: Cambridge, UK, 2011. [CrossRef]
22. Wiser, R.; Yang, Z.; Hand, M.; Hohmeyer, O.; Infield, D.; Jensen, P.H.; Nikolaev, V.; O'Malley, M.; Sinden, G.; Zervos, A. Wind Energy. In *Renewable Energy Sources and Climate Change Mitigation: Special Report of the Intergovernmental Panel on Climate Change*; Edenhofer, O., Pichs-Madruga, R., Sokona, Y., Seyboth, K., Kadner, S., Zwickel, T., Eickemeier, P., Hansen, G., Schlömer, S., von Stechow, C., et al., Eds.; Cambridge University Press: Cambridge, UK, 2011; pp. 535–608. [CrossRef]
23. Global Wind Energy Council. *Global Wind Report 2023*; Technical Report; Global Wind Energy Council: Brussels, Belgium, 2023. Available online: https://gwec.net/globalwindreport2023/ (accessed on 23 September 2026).
24. Burton, T.; Sharpe, D.; Jenkins, N.; Bossanyi, E. *Wind Energy Handbook*; John Wiley & Sons: Chichester, UK, 2001. [CrossRef]
25. Armstead, H.C.H. *Geothermal Energy: Its Past, Present, and Future Contributions to the Energy Needs of Man*, 2nd ed.; E. & F. N. Spon: London, UK, 1983; pp. 1–289.
26. Kalay, M.Ş.; Kılıç, B.; Sağlam, Ş. Systematic Review of the Data Acquisition and Monitoring Systems of Photovoltaic Panels and Arrays. *Sol. Energy* **2022**, *244*, 47–64. [CrossRef]
27. Tautz-Weinert, J.; Watson, S.J. Using SCADA Data for Wind Turbine Condition Monitoring—A Review. *IET Renew. Power Gener.* **2017**, *11*, 382–394. [CrossRef]
28. García Márquez, F.P.; Peinado Gonzalo, A.; Papaelias, M. A Comprehensive Review of Condition Monitoring Systems for Hydropower Stations: Technologies, Applications, and Future Trends. *Electr. Power Syst. Res.* **2026**, *251*, 112339. [CrossRef]
29. Prauzek, M.; Kucova, T.; Konecny, J.; Adamikova, M.; Gaiova, K.; Mikus, M.; Pospisil, P.; Andriukaitis, D.; Zilys, M.; Martinkauppi, B.; et al. IoT Sensor Challenges for Geothermal Energy Installations Monitoring: A Survey. *Sensors* **2023**, *23*, 5577. [CrossRef] [PubMed]

30. Güney, E.; Demir, M. Time-Aware Machine Learning for Biomass Power Output Estimation Using SCADA Data. *Arab. J. Sci. Eng.* **2026**, *51*, 18663–18675. [CrossRef]
31. *IEC 61850-5:2013*; Communication Networks and Systems for Power Utility Automation—Part 5: Communication Requirements for Functions and Device Models. Edition 2.0; International Electrotechnical Commission: Geneva, Switzerland, 2013.
32. Araniti, G.; Iera, A.; Pizzi, S.; Rinaldi, F. Toward 6G Non-Terrestrial Networks. *IEEE Netw.* **2022**, *36*, 113–120. [CrossRef]
33. GSMA. *High Altitude Platform Systems: Towers in the Skies, Version 2.0*; White Paper; GSMA: London, UK, 2022. Available online: https://www.gsma.com/futurenetworks/gsma_resources/high-altitude-platform-systems-towers-in-the-skies-version-2-0/ (accessed on 23 September 2026).
34. Vaezi, M.; Azari, A.; Khosravirad, S.R.; Shirvanimoghaddam, M.; Azari, M.M.; Chasaki, D.; Popovski, P. Cellular, Wide-Area, and Non-Terrestrial IoT: A Survey on 5G Advances and the Road Toward 6G. *IEEE Commun. Surv. Tutor.* **2022**, *24*, 1117–1174. [CrossRef]
35. Plastras, S.; Tsoumatidis, D.; Skoutas, D.N.; Rouskas, A.; Kormentzas, G.; Skianis, C. Non-Terrestrial Networks for Energy-Efficient Connectivity of Remote IoT Devices in the 6G Era: A Survey. *Sensors* **2024**, *24*, 1227. [CrossRef] [PubMed]
36. Demircioglu, E.; Ertok, H.H.; Çankaya, İ.; Sözbir, N. Non-Terrestrial Network Concepts in 5G and Beyond Communication Technologies. *Duzce Univ. J. Sci. Technol.* **2024**, *12*, 1930–1943. [CrossRef]
37. Nguyen, C.T.; Saputra, Y.M.; Huynh, N.V.; Nguyen, T.N.; Hoang, D.T.; Nguyen, D.N.; Pham, V.Q.; Voznak, M.; Chatzinotas, S.; Tran, D.H. Emerging Technologies for 6G Non-Terrestrial Networks: From Academia to Industrial Applications. *IEEE Open J. Commun. Soc.* **2024**, *5*, 3852–3885. [CrossRef]
38. Rinaldi, F.; Määttänen, H.L.; Torsner, J.; Pizzi, S.; Andreev, S.; Iera, A.; Koucheryavy, Y.; Araniti, G. Non-Terrestrial Networks in 5G & Beyond: A Survey. *IEEE Access* **2020**, *8*, 165178–165200. [CrossRef]
39. Kodheli, O.; Maturo, N.; Andrenacci, S.; Chatzinotas, S.; Zimmer, F. Link Budget Analysis for Satellite-Based Narrowband IoT Systems. In *Proceedings of the Ad-Hoc, Mobile, and Wireless Networks*; Palattella, M.R., Scanzio, S., Coleri Ergen, S., Eds.; Lecture Notes in Computer Science; Springer: Cham, Switzerland, 2019; Volume 11803, pp. 259–271. [CrossRef]
40. Guidotti, A.; Vanelli-Coralli, A.; Mengali, A.; Cioni, S. Non-Terrestrial Networks: Link Budget Analysis. In Proceedings of the 2020 IEEE International Conference on Communications (ICC), Dublin, Ireland, 7–11 June 2020; pp. 1–7. [CrossRef]
41. *IEC 60870-5-104:2006*; Telecontrol Equipment and Systems—Part 5-104: Transmission Protocols—Network Access for IEC 60870-5-101 Using Standard Transport Profiles. Edition 2.0. International Electrotechnical Commission: Geneva, Switzerland, 2006.
42. Banks, A.; Briggs, E.; Borgendale, K.; Gupta, R. MQTT Version 5.0. OASIS Standard, OASIS: Burlington, MA, USA, 2019. Available online: https://docs.oasis-open.org/mqtt/mqtt/v5.0/mqtt-v5.0.html (accessed on 23 September 2026).
43. Shelby, Z.; Hartke, K.; Bormann, C. *The Constrained Application Protocol (CoAP)*; RFC 7252; Internet Engineering Task Force (IETF): Fremont, CA, USA, 2014. [CrossRef]
44. Jha, A.V.; Appasani, B.; Ghazali, A.N.; Pattanayak, P.; Gurjar, D.S.; Kabalci, E.; Mohanta, D.K. Smart Grid Cyber-Physical Systems: Communication Technologies, Standards and Challenges. *Wirel. Netw.* **2021**, *27*, 2595–2613. [CrossRef]
45. ITU-R. *Propagation Data Required for the Design Systems in the Land Mobile-Satellite Service*; Recommendation ITU-R P.681-11; International Telecommunication Union: Geneva, Switzerland, 2019.
46. The MathWorks, Inc. NB-IoT NTN Link Budget Analysis, Satellite Communications Toolbox Documentation. Available online: https://www.mathworks.com/help/satcom/ug/nb-iot-ntn-link-budget-analysis.html (accessed on 23 September 2026).
47. 3GPP. *Evolved Universal Terrestrial Radio Access (E-UTRA); Physical Layer Procedures*; Technical Specification 3GPP TS 36.213 V17.5.0 (Release 17); 3rd Generation Partnership Project (3GPP): Sophia Antipolis, France, 2023.
48. The MathWorks, Inc. NB-IoT NTN NPDSCH Throughput, LTE Toolbox Documentation. Available online: https://www.mathworks.com/help/lte/ug/nb-iot-ntn-npdsch-throughput.html (accessed on 23 September 2026).
49. 3GPP. *Evolved Universal Terrestrial Radio Access (E-UTRA); Physical Channels and Modulation*; Technical Specification 3GPP TS 36.211 V17.3.0 (Release 17); 3rd Generation Partnership Project (3GPP): Sophia Antipolis, France, 2023.

Disclaimer/Publisher's Note: The statements, opinions and data contained in all publications are solely those of the individual author(s) and contributor(s) and not of MDPI and/or the editor(s). MDPI and/or the editor(s) disclaim responsibility for any injury to people or property resulting from any ideas, methods, instructions or products referred to in the content.